Methods in Geochemistry and Geophysics

ELECTROMAGNETIC SOUNDING OF THE EARTH'S INTERIOR

THEORY, MODELING, PRACTICE

Edited by VIACHESLAV V. SPICHAK

SECOND EDITION

Electromagnetic Sounding of the Earth's Interior: Theory, Modeling, Practice

Electromagnetic Sounding of the Earth's Interior: Theory, Modeling, Practice

Second Edition

Viacheslav V. Spichak
Geoelectromagnetic Research Center IPE RAS, Moscow, Russia

AMSTERDAM • BOSTON • HEIDELBERG • LONDON
NEW YORK • OXFORD • PARIS • SAN DIEGO
SAN FRANCISCO • SINGAPORE • SYDNEY • TOKYO

Elsevier
Radarweg 29, PO Box 211, 1000 AE Amsterdam, Netherlands
The Boulevard, Langford Lane, Kidlington, Oxford OX5 1GB, UK
225 Wyman Street, Waltham, MA 02451, USA

Notices

Knowledge and best practice in this field are constantly changing. As new research and experience broaden our understanding, changes in research methods, professional practices, or medical treatment may become necessary.

Practitioners and researchers must always rely on their own experience and knowledge in evaluating and using any information, methods, compounds, or experiments described herein. In using such information or methods they should be mindful of their own safety and the safety of others, including parties for whom they have a professional responsibility.

To the fullest extent of the law, neither the Publisher nor the authors, contributors, or editors, assume any liability for any injury and/or damage to persons or property as a matter of products liability, negligence or otherwise, or from any use or operation of any methods, products, instructions, or ideas contained in the material herein.

British Library Cataloguing-in-Publication Data
A catalogue record for this book is available from the British Library

Library of Congress Cataloging-in-Publication Data
A catalog record for this book is available from the Library of Congress

ISBN: 978-0-444-63554-9

Typeset by Thomson Digital

Chapter 3

Shallow Investigations by TEM-FAST Technique: Methodology and Examples

Pavel O. Barsukov, Edward B. Fainberg, and Eugene O. Khabensky
Lab EM Methods and Technologies for Environmental Studies, Geoelectromagnetic Research Center IPE RAS, Moscow, Russia

Chapter Outline

3.1 INTRODUCTION

In recent years, geophysical methods became widely used by geologists, engineers, hydrogeologists, and other specialists in geotechnical, hydrogeological, and archaeological studies, in the environment monitoring and for other purposes. High ranking among these studies are shallow depth investigations. Generally speaking, contemporary geoelectrics provides tools for studying the electrical conductivity distribution from the Earth surface down to the depth of dozen and hundred kilometers. Within the depth interval down to ten meters, GPR works quite well; the DC methods of electric prospecting (VES) are effective in the depth range 30–50m. Depth interval from 500 m to a few hundred kilometers is studied mostly by magnetotelluric methods.

Electromagnetic Sounding of the Earth's Interior: Theory, Modeling, Practice
http://dx.doi.org/10.1016/B978-0-444-63554-9.00003-9

The depths of interest for our study lie within an interval between ~5 and 10 m to a few hundred meters. This is just the region where everyday human activity is running, and just to that region the main emphasis of electric prospecting is gradually tending.

Electric prospecting methods are usually divided into those employing either the direct (DC) or alternating (AC) current. Advantage of DC methods is high sensitivity to local inhomogeneities, especially high-resistivity ones. However, this advantage turns a shortcoming if the survey is purposed on the study of layers and objects overlaid by near-surface inhomogeneities and highly resistive layers. In such cases, efficiency of DC methods drops, and analysis and interpretation of the obtained results become considerably more difficult. Methods based on the use of alternating current relate to the so called "induction methods."

3.2 ADVANTAGES OF TEM IN SHALLOW DEPTH STUDIES

The vertical electric sounding method using direct current (VES DC), proposed by Schlumberger (1920), and the transient electromagnetic method (TEM) with short source-receiver offsets proposed by Obukhov (1968) are the most widely used methods of the earth prospecting within the depth range of 300–500 m. Both methods have advantages and disadvantages.

The VES DC method has approximately the equal sensitivity with respect to high and low resistive targets, at that, the sounding depth is controlled by the source-receiver offset. However, to achieve the desired sounding depth, the DC method requires the offsets of 5–6 times the depth.

The TEM method operates in the near field of the source, at that the sounding depth is controlled by the diffusion depth depending on the transient time. In favorable conditions, the use of transmitting-receiving magnetic antennas (loops), the sounding depth, is usually 3–4 times their size. This advantage allows exploring the complex geological media with high locality and depth. However, the transient responses in magnetic loops are less sensitive to high resistive objects and cannot be effectively used for sounding of geological structures comprising thin resistive layers.

Figure 3.1 shows the apparent resistivity curves for VES-DC and TEM responses, calculated for a layered one-dimensional (1-D) section.

The circular labels denote the range of the offsets and the transients defining the section. It is seen that to reach the depth of ~100 m, one needs the VES AB = 600 m, while for TEM method, the loop of 25×25 m^2 size is enough to measure the transients in the time range of $t \leq 800$ μs. Within this range the normalized amplitude of the response is $\sim 5 \times 10^{-6}$ V/A, and there is no problem to measure it. In the sections close to the horizontally homogeneous, the DC methods allow to get acceptable results in a wide range of resistivity and thickness of layers. However, in complex three-dimensional (3-D) structures the possibilities of DC methods are significantly reduced.

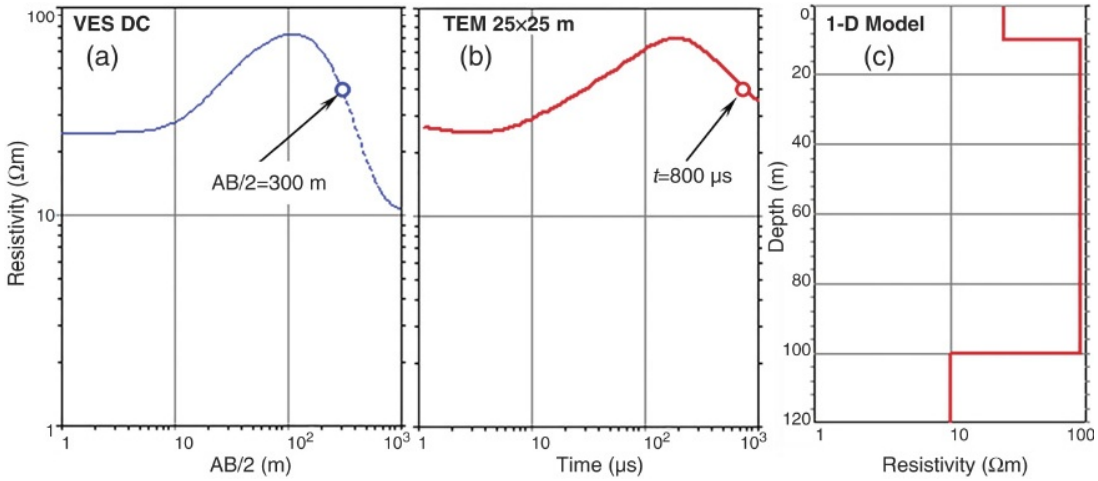

FIGURE 3.1 (a) VES DC and (b) TEM responses in the apparent resistivity form calculated for (c) a three-layered 1-D model. The transmitting-receiving loop is of 25 × 25 m^2 size. The labels denote the range of the offsets and the transients sufficient to define the true section.

3.3 ON THE TEM-FAST TECHNOLOGY

In the TEM-FAST technology, a single square or rectangular loop is used as the transmitting and receiving antennae (the so called a single-loop TEM configuration). This enables three purposes to be reached at the same time: first, time variations of the magnetic flux through the loop are measured, and the effects of subsurface irregularities in the antenna vicinity are integrated maximally; second, efficiency of the field experiment grows significantly since a second loop placement or induction receiver installation is no longer necessary; and third, the measured transient process shows a series of unique helpful peculiarities used in performing the transformations.

Most important characteristic feature of any TEM equipment is the duration of self-transient process, that is, of the process dependent on the transmitter-antenna-receiver system properties. It is obvious that proper quality TEM signal measurements are feasible only within the time interval where the self-transient process of the system is missing. The shorter it is the earlier are the time delays when measurements become feasible and the less is the minimum depth of study. The voltage and the current in a loop at small times depend on the loop size, its resistance, capacitance, inductance, and show quite a complicated behavior. Figure 3.2 shows examples of the voltage and current in the TEM-FAST 48HPC antennas of 50 × 50 m^2 and 20 × 20 m^2 measured by Tektronix (THS 720) oscillograph after switching off current in TEM-FAST 48HPC antennas. For comparison, in the Figure 3.2, there is also the voltage calculated from formulas for a line with distributed parameters. Figure 3.3 shows the current in antennas calculated from the oscillogram.

Signal measurement and processing are carried out via a portable computer that monitors the equipment condition, operation process, and data quality, and,

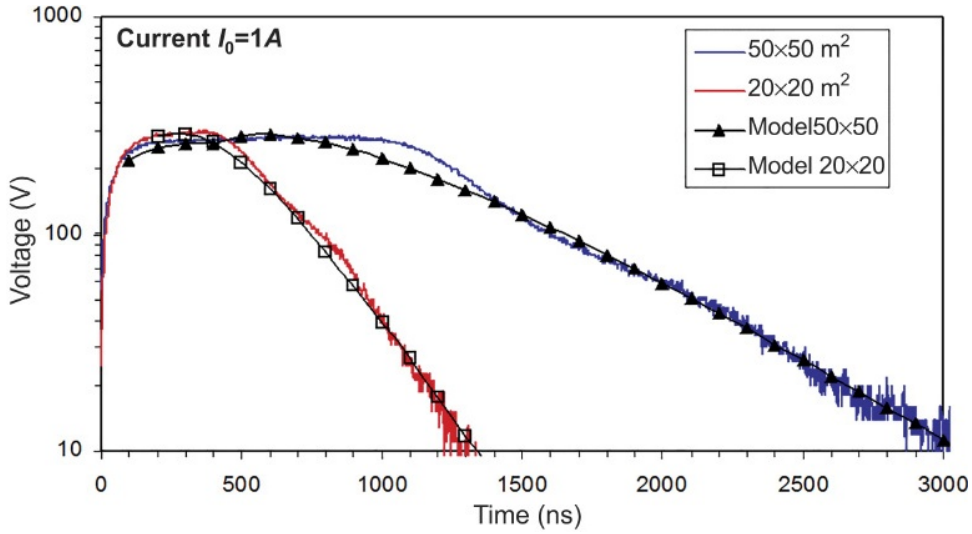

FIGURE 3.2 "Step-off" voltage in the antennas measured by Tektronix (THS 720) oscillograph. The current before "Off" is 1 A. The model curves are voltage calculated for lines with distributed parameters.

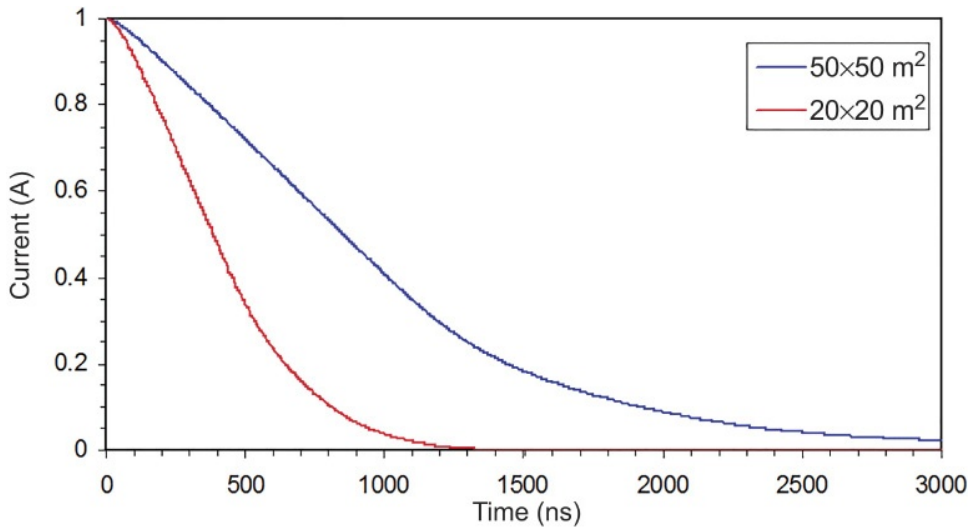

FIGURE 3.3 Dependence of the current's decay rate on the size of antennas.

in accordance with a special code, carries out signal stacking to provide the best signal to noise ratio. Simultaneously, with measurements of the medium response at each time lag, also electromagnetic noise is measured (Figure 3.4), which is important for data filtering and the inverse problem solution.

In the process of measurements, the quality of obtained data is controlled by the operator: the graphs of transient field and apparent resistivity curves with errors are constructed, and in the cases when errors are unacceptably large, the procedure is changed (accumulation amount, size of the antenna, the current value), and repeated.

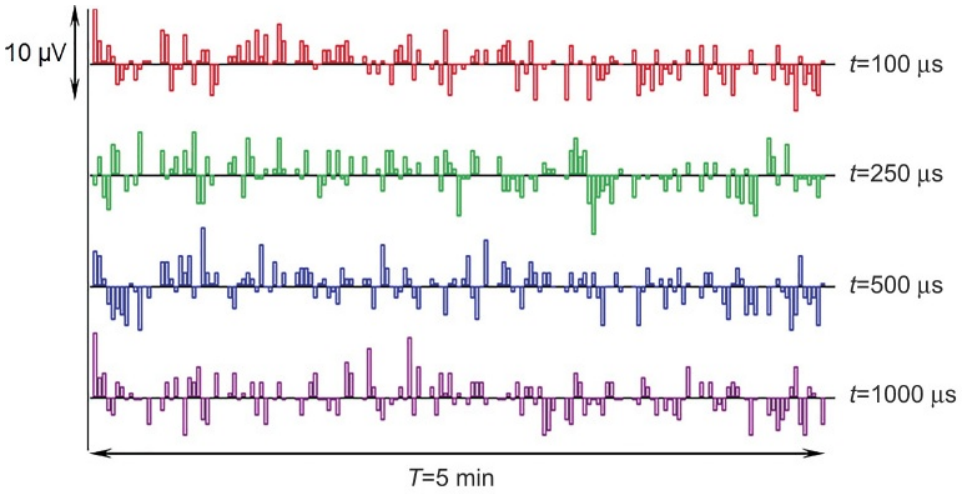

FIGURE 3.4 Example of an external electromagnetic noise induced in the receiving antenna within 5 min.

3.4 1-D MODELING AND INVERSION

3.4.1 Modeling

Fundamental model underlying the graphical representations of the measured data and the construction of the simplest models is a layered half-space, consisting of one or a plurality of horizontally homogeneous layers. The theory of propagation of the electromagnetic field in this model is well known (Obukhov, 1968; Sidorov and Tikshaev, 1969; Kamenetsky et al., 2010) and is widely used for solving the direct 1-D problem. Common practice in the electric prospecting is to use, as the interpretation parameter, an apparent resistivity $\rho_a(t)$ of a homogeneous medium the response of which at a given time coincides with the signal measured in experiment. Traditionally (Obukhov, 1968), $\rho_a(t)$ is calculated by asymptotic formula for late times in the near field of the source when the condition $t/[\mu_0 R^2/\rho_a(t)] >> 1$ is satisfied:

$$\rho_a(t) = \left[\frac{\sqrt{\pi}}{20}\frac{\mu^{5/2}R^4}{t^{5/2}E(t)/I}\right]^{2/3} \tag{3.1}$$

Here, $E(t)/I$ is the measured value of normalized voltage at antenna terminals, and $R = L/\pi^{1/2}$ is effective radius of a single-turn square antenna with a side L.

However, it is possible to introduce an apparent resistivity $\rho_f(t)$ calculated from the complete formula for the field valid at any stage of the transient process: in the near, middle, and far field. According to Lee (1981), the voltage in a single-loop antenna for a homogeneous half-space equals to:

$$E(t)/I = \pi\mu R^2 \int_0^\infty \frac{e^{-t/\tau}}{\tau}\left[\frac{1}{\sqrt{\pi t/\tau}} - e^{t/\tau}\,erfc(\sqrt{t/\tau})\right] J_1^2(\lambda r)d\lambda\,,\quad \tau = \frac{1}{\rho}\frac{\mu}{\lambda^2} \tag{3.2}$$

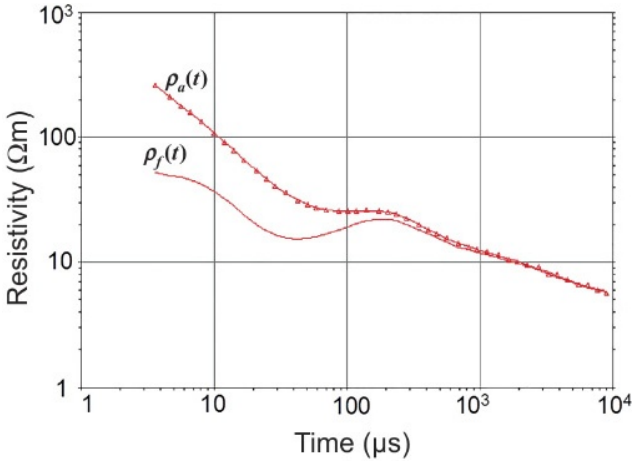

FIGURE 3.5 Apparent resistivity calculated by asymptotic $\rho_a(t)$ and general (3.2) formulas.

Apparent resistivity, $\rho_f(t)$, can be obtained by solving the equation (3.2), on the left-hand side of which there is the measured voltage. Apparent resistivities calculated from asymptotic formula for the near field (3.1) and from general formula (3.2) coincides at late times and essentially differ at earlier times when $t/(\mu_0 R^2/\rho_a(t)) < 1$ (Figure 3.5).

Note that $\rho_f(t)$, in contrast to $\rho_a(t)$ does not distort the shape of apparent resistivity at all stages of the transient process. Reconstruction of the section from the apparent resistivity curves (that are a usual form of the field data representation) is carried out by either by solving the inverse problem in a class of layered media or by the transformation of the curves (in this case, a gradient section is calculated). Although, both the approaches have their own inherent significance and can be applied independently, quite often it is helpful to use the transformation results in constructing the initial model for inverse problem solution in a class of layered media.

3.4.2 Transformation

The results of TEM-FAST measurements $E(t)/I$ can be transformed directly to the $\rho(h)$ dependence. Combining such dependencies along a profile, one can construct a two-dimensional (2-D) section. Sometimes this transformation is referred to as "imaging." Transformation $E(t)/I \rightarrow \rho(h)$ in TEM-FAST follows the ideas of well-known Berdichevsky, Niblett, Bostick, Molochnov, Le-Vyet transformations (Berdichevsky and Dmitriev, 1992)[1] of MT data, but has some peculiarities permitting to adjust the $\rho(h)$ resolution depending on the type and contrast of variations in the geoelectric cross-section section under study. For the $E(t)/I \rightarrow \rho(h)$ transform, two functions are employed: the apparent resistivity $\rho_f(t)$ determined by complete formula, and its time derivative $d\rho/dt = \rho'_f(t)$. The procedure of $\rho_f(t)$ and $\rho'_f(t)$ calculation (solution of equation (3.2)) relate to the class of unstable problems and

1. See also Chapter 11 (Ed.).

require a special algorithm for smoothing the initial data $E(t)/I$. The smoothing algorithm is described in detail in (Svetov and Barsukov, 1984) and based on the transient process $E(t)$ representation as a superposition of exponent functions:

$$E(t) = \int_0^\infty E(s)e^{-st}\,ds, \tag{3.3}$$

where the real function $E(s)$ of a real exponent s is called an exponential spectrum. The use of additional information about the spectrum $E(s)$ behavior essentially increases the stability of a solution. For example, in a single-loop TEM configuration, irrespectively of the given distribution pattern of frequency-independent conductivity in the medium, the exponential spectrum is positive for any values of s, from which it follows that the transient signals $E(t)$ themselves and all their time derivatives have a property of "perfect monotony" (Gubatenko and Tikshaev, 1979; Weidelt, 1982).

$$\frac{d^nE(t)}{dt^n} = (-1)^n \int_0^\infty s^nE(s)e^{-st}\,ds, \qquad (-1)^n\frac{d^nE(t)}{dt^n} > 0, \qquad n \geq 0, t > 0 \tag{3.4}$$

This means that the transient process cannot change its polarity, neither its time derivatives change their sign. But if the signal measured in a single-loop antenna decreases nonmonotonically with changing its polarity, this unambiguously speaks for the frequency dependency of the studied medium (induced polarization, or IP-effect).

Thus, first, the experimental data are smoothed (the approximation by superposition of exponent functions in accordance to equation (3.3)), and then the apparent resistivity $\rho_f(t)$ is calculated by the formula (3.2). After that, the correcting coefficient $k(t)$ is determined as:

$$k(t) = \frac{1}{(1-\nu)^{3/2}}, \qquad \nu = \frac{t}{\rho_f(t)}\frac{d\rho_f(t)}{dt} = \frac{d\ln\rho_f(t)}{d\ln t}, \qquad \mathrm{abs}(\nu) < 1 \tag{3.5}$$

Then $\rho(h)$ and effective depth of sounding h for each time t can be found as:

$$\rho(h) = k(t)\rho_f(t), \qquad h = \sqrt{\frac{t\beta(\mathrm{res})}{\mu_0}}. \tag{3.6}$$

$$\ln(\beta(res)) = \ln(\rho_m) + \frac{\ln(\rho_h) - \ln(\rho_m)}{10}\cdot res, \;\; 0 \leq res \leq 10.$$

The function $\beta(\mathrm{res})$ has the dimension of Ωm and can vary from the value ρ_f of "untransformed" resistivity to the value of ρ_h of (3.6). Variations in $\beta(\mathrm{res})$ significantly change the shape of the curve $\rho_h = \rho(h)$ and the resolving power of transformations. For low contrast media $\beta \to \rho_h$, for the higher contrast ones $\beta \to \rho_f$, for intermediate contrast media $\beta = (\rho_h\,\rho_m)^{1/2}$.

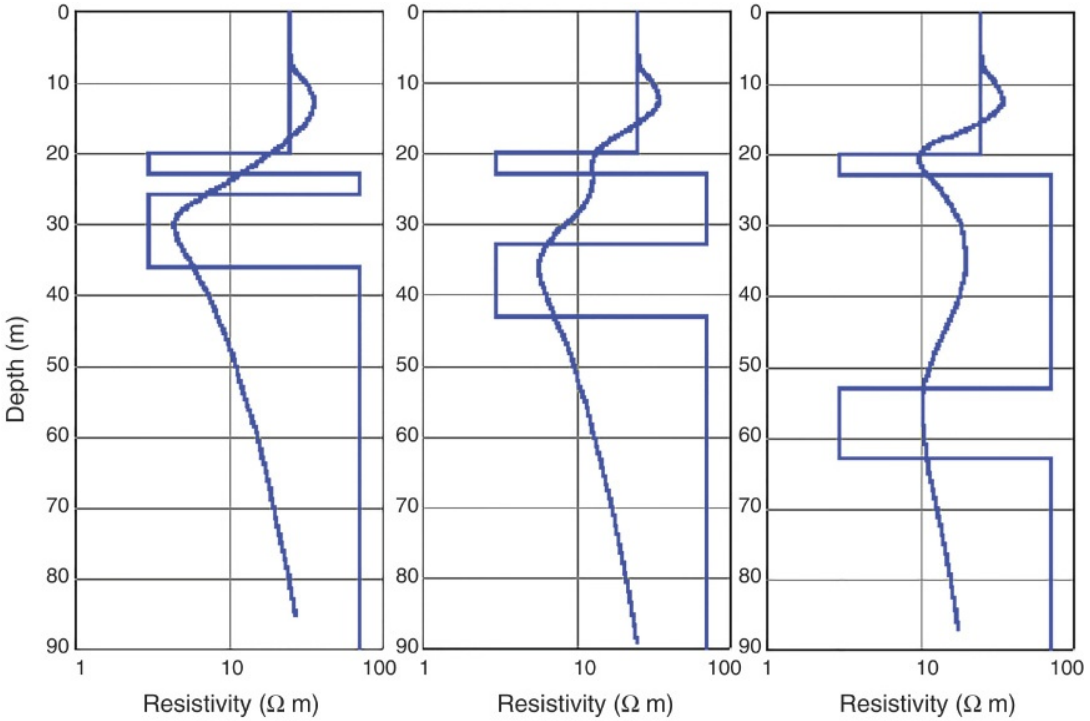

FIGURE 3.6 Example of $\rho_a(t) \rightarrow \rho(h)$ transformation. Interlayer spacing for left, middle, and right panel is 3, 10, and 30 m, respectively.

Relation between ρ_h and ρ_m in β(res) is controlled by a specific parameter resolution "res" (resolving power of the transformation), which can be changed either manually or automatically via the transformation program.

Reconstruction of $\rho(h)$ section is carried out automatically without involving any additional information. Since it is not necessary to specify the number of layers in $\rho(h)$ calculation, the reconstructed sections, in spite of their being actually the pseudosections, in many cases reproduce the resistivity distribution with depth more adequately than the data inversion in the class of layered media.

Figure 3.6 illustrates the changes in the resolving power of transformations with the spacing between two thin high-conductive clay layers (ρ = 3 Ωm) imbedded in high-resistive rocks (ρ = 70 Ωm). At a spacing h = 3 m the layers are indistinguishable; resolution increases with the increasing spacing of layers.

Figure 3.7 shows a model example of visualization of the section according to the profile "measurements."

After pointwise transformation and stitching of 1-D sections in the 2-D image we obtain the image qualitatively reflecting the most important features of the section.

3.4.3 Inversion

1-D inversion in the class of layered models is the next step after visualization of the section. The values of resistivity and layer thickness are calculated from the minimum of the misfit functional of calculated and experimental data. The choice of the initial model is based on the available information about the section or, as shown in Figure 3.8, on the pseudo-section $\rho(h)$.

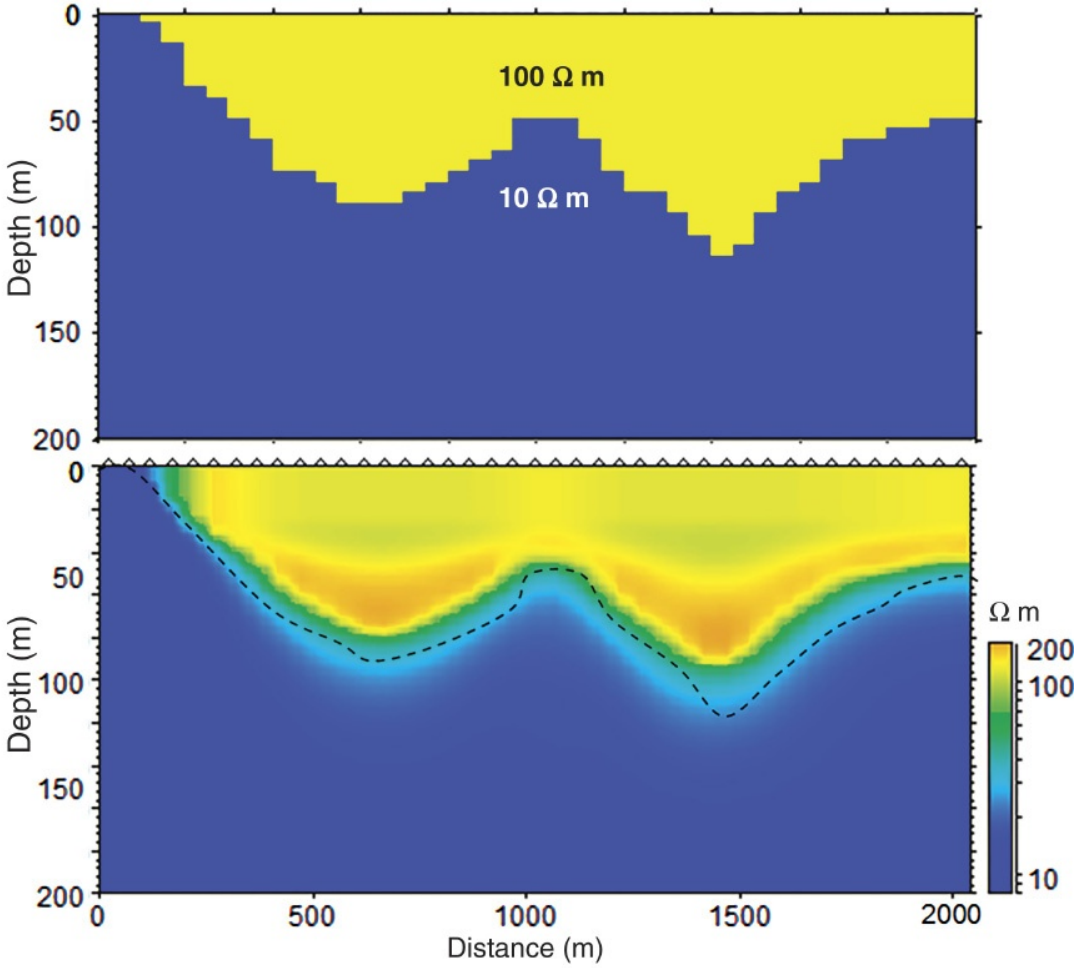

FIGURE 3.7 Complex 2-D structure (top panel) and its visualization by the transformation of $E(t)$ to $\rho(h)$ (lower panel). The dotted line represents the contour of the "true" structure.

1-D inversion is performed numerically by well-known Levenberg–Marquardt method (Commer et al., 2003). According to this scheme, at each iteration, the model correction quantity $\delta\mathbf{p}$ is derived as

$$\delta\mathbf{p} = \mathrm{W}^2(\mathbf{J}^T\mathrm{W}^2\mathbf{J} + \beta\mathbf{I})^{-1}\mathbf{J}^T\delta\mathbf{d} \tag{3.7}$$

Here, $\mathbf{I}$ denote the identity matrix and $\delta\mathbf{d}$ is the data misfit vector between the observed and prediction data calculated at the current iteration. The Jacobian $\mathbf{J}$ represents the partial derivatives of the predicted data with respect to the model parameters $\mathrm{J}_{ij} = \partial \mathrm{d}_i/\partial \mathrm{p}_j$, $i = 1,..., N$; $j = 1, ..., M$, where N is the number of measurements and M is the number of unknown model parameters. The size of $\mathbf{J}$ is $N \times M$. The $\beta\mathbf{I}$ member in (3.7) is a regularizator controlling the damping of the solution. It prevents the potential singularity of $\mathbf{J}^T\mathbf{J}$ by adding a constant to its main diagonal. The weight matrix W is introduced to take into account the errors of experimental data. The errors are determined as the standard deviation for each measuring point and at each time.

In the case of array studies, a necessity emerges of automatic inversion of rather large volumes of TEM-FAST data (a few thousands of transient sounding

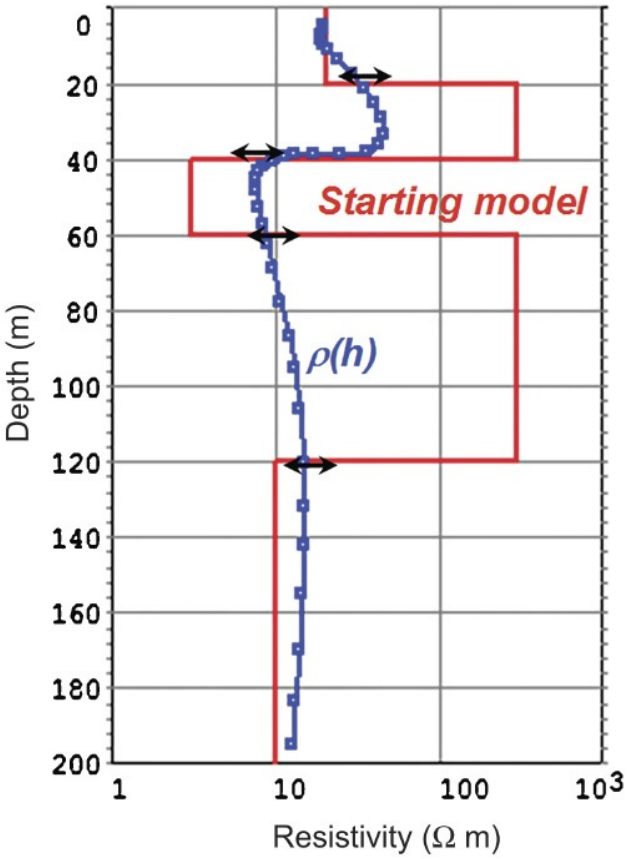

FIGURE 3.8 Determination of the starting model in 1-D inversion. Horizontal arrows in the curve correspond to the depths where the second depth derivative of $\rho(h)$ is equal to zero (knee points).

points). A special algorithm is provided to solve this problem. This algorithm stabilizes the inversion procedure by using, as an initial model at each point, the inversion result at neighboring points of the studied area. In addition, to obtain geologically adequate result of the inversion, it is necessary to constrain the values of resistivity and layers' thickness with all ever-possible accuracy. An example of automatic inversion of TEM data measured at kimberlite prospecting in Russia is presented in Figure 3.9 as mean resistivity of layers of 10-m thick at depths of 50, 100, and 200 m. Inversion was carried out for a case of five-layer section with resistivity ranging from 10 Ωm to 300 Ωm. The high resistivity layer was discovered at the depth of 150–200 m.

3.5 3-D MODELING AND INVERSION

3.5.1 Modeling

In many cases, 1-D transformation and inversion with following stitching of the pointwise sections in 2-D and 3-D pseudo-sections is sufficient for the research purposes. However, sometimes, when the sections and the targets under exploration are clearly 3-D, it is necessary to carry out 3-D modeling and inversion to receive correct geometry and resistivity of the section under consideration.

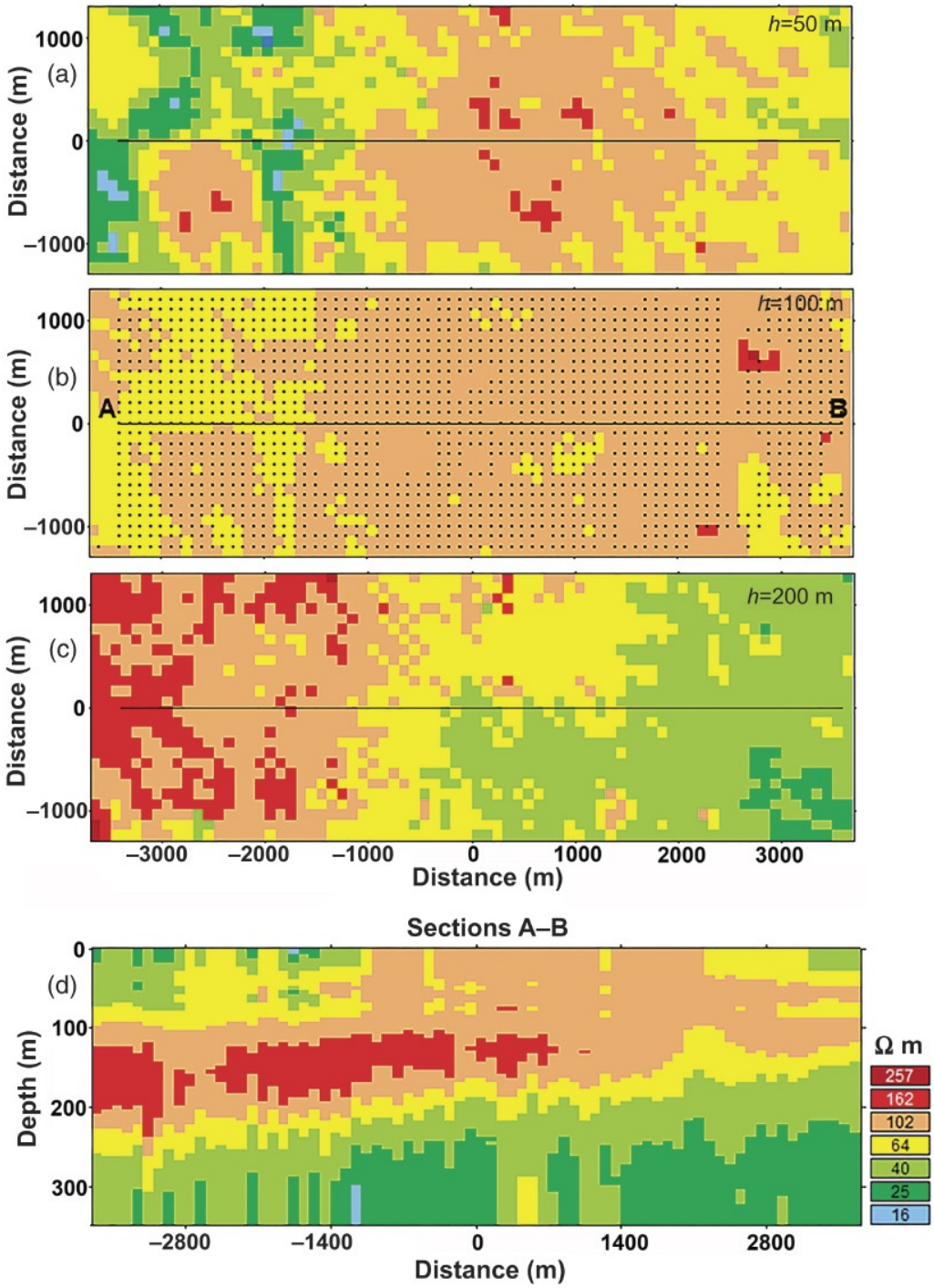

FIGURE 3.9 1-D inversion of the real TEM-FAST data (3500 soundings with 100 × 100 m^2 antenna, Russia). The (a–c) panels show the horizontal section of resistivities (in Ωm) at 50, 100, and 200 m. The d panel shows the vertical resistivity sections along A–B profile.

The modified 3-D algorithm of Druskin and Knizhnerman (1988) giving possibility to calculate electromagnetic field at many points at once without a significant increase of computer time is used in TEM-FAST technology. The modification consists of the grids construction based on the features of the model under consideration; the accuracy of computations is controlled by the calculations at successively nested grids and asymptotic to early and

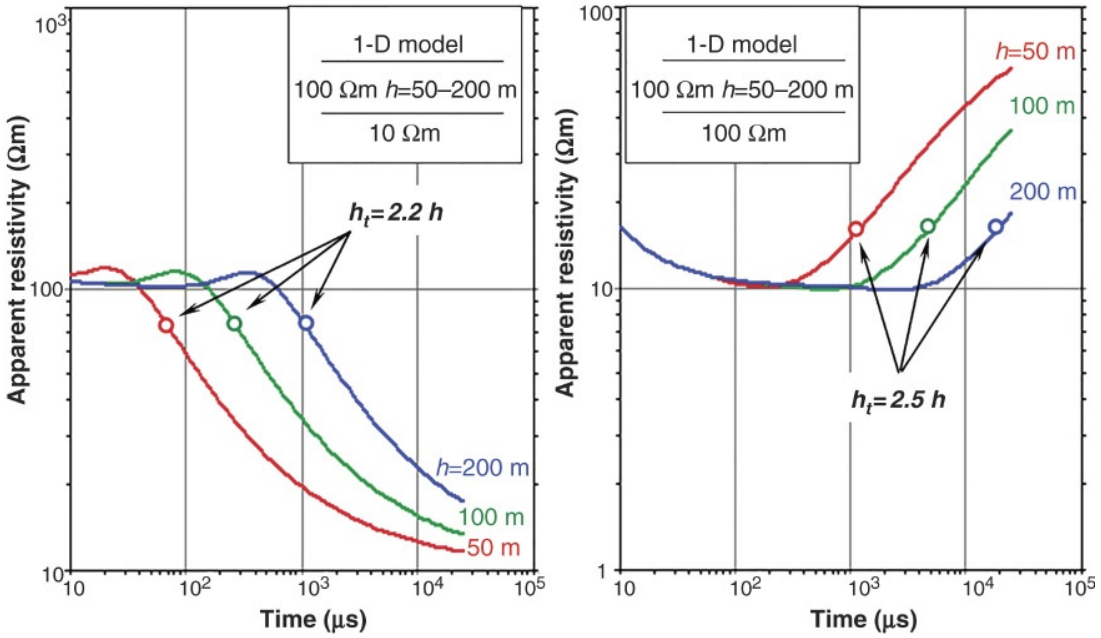

FIGURE 3.10 The apparent resistivity curves for a two-layered medium. The circular labels mark the transient times where the resistivity is 1.5 times less or greater the resistivity of the upper layer.

later times. The computational algorithm is adapted for parallel calculations on multicore desktop or notebook computers.

Figure 3.10 presents the apparent resistivity curves for two 1-D models comprising two layers of 100 Ωm and 10 Ωm resistivity with thickness of 50, 100, and 200 m. The points labeled by circles lie on the down and upward asymptotes of the apparent resistivity curves, indicating the existence of low and high resistive layers in the base of the section.

Having responses measured within the time range limited by these points, one can uniquely define all parameters of the model. The diffusion depth $h_t = (2\rho t / \mu)^{1/2}$, corresponding to the marked transient times and resistivity of upper layers, is $h_t = 2.2h$ and $h_t = 2.5h$; here h is a thickness of the upper layer. Thus, the sounding depths (i.e., the thickness of the upper layer) in the considered models is 2.2 and 2.5 times less than the diffusion depth.

Figure 3.11 presents the apparent resistivity curves for two 3-D models, comprised of a circular cylinder of radius R and height h = 100 m, and resistivity of 100 and 10 Ωm, placed in a uniform half-space with resistivity of 10 and 100 Ωm, respectively.

These models allow estimating the lateral locality of TEM sounding. The responses of 3-D and 1-D models coincide at all times not exceeding the labeled one, if the radius R of cylinder equal to diffusion depth ($R = h_t$, left panel) or exceeds it two times ($R = 2h_t$, right panel). Thus, the side effects caused by high-resistive enclosed strata are negligible if they are located at distances more than two diffusion depths. If the side effects are caused by low resistive medium, the allowable range is equal to diffusion depth.

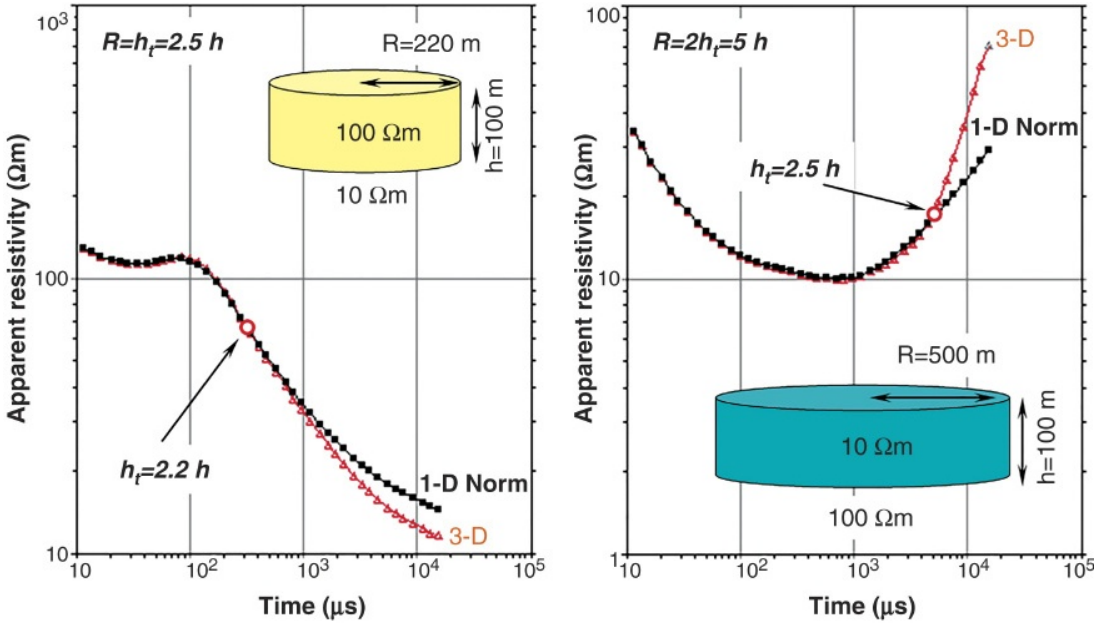

FIGURE 3.11 The apparent resistivity curves for 3-D models containing cylindrical inclusions. The circular labels mark the points on the downward and upward asymptotic branches of the curves used for evaluation of the diffusion depth of the field. Black curves "1-D Norm" correspond to the 1-D model shown in Figure 3.11 at h = 100 m.

The following example shows the profiles of transient responses for a model consisting of two half-spaces of 10 and 100 Ωm resistivity (Figure 3.12). As can be seen, the mutual influence of half-spaces ends at a distance from the boundary approximately equal to the diffusion depth h_t.

3-D modeling is a good tool for assessing of resolution and evaluation of the section's parameters accuracy. This possibility is illustrated by the Figure 3.13 where the series of four simplified 3-D models of kimberlite pipes of 100 × 100–400 × 400 m^2 size embedded in 100 Ωm sediments are presented. The depth of the pipe is half of its size.

The panels (b) and (c) show the 1-D pointwise inversion and transformation, respectively. As one can see, the transformation's image reflects the boundaries of the layers and kimberlites better than the 1-D inversion. At the same time both methods overestimate size of the kimberlite bodies and their resistivity at least 10–20 Ωm instead of 3 Ωm. In some cases such inaccuracy is unacceptable, for example at fresh water exploration or estimation of its mineralization.

3.5.2 Inversion

The measured data are disturbed by the heterogeneities, and, in many cases, these errors are impossible to quantify. However, if the data are measured on the sufficiently long profiles (or over sufficiently large areas), it is quite natural that the interpreter desires to retrieve the geoelectric models of the medium simultaneously for the entire volume under study. Constructing the starting 2-D or 3-D models of the medium from the local 1-D transformations does not present any

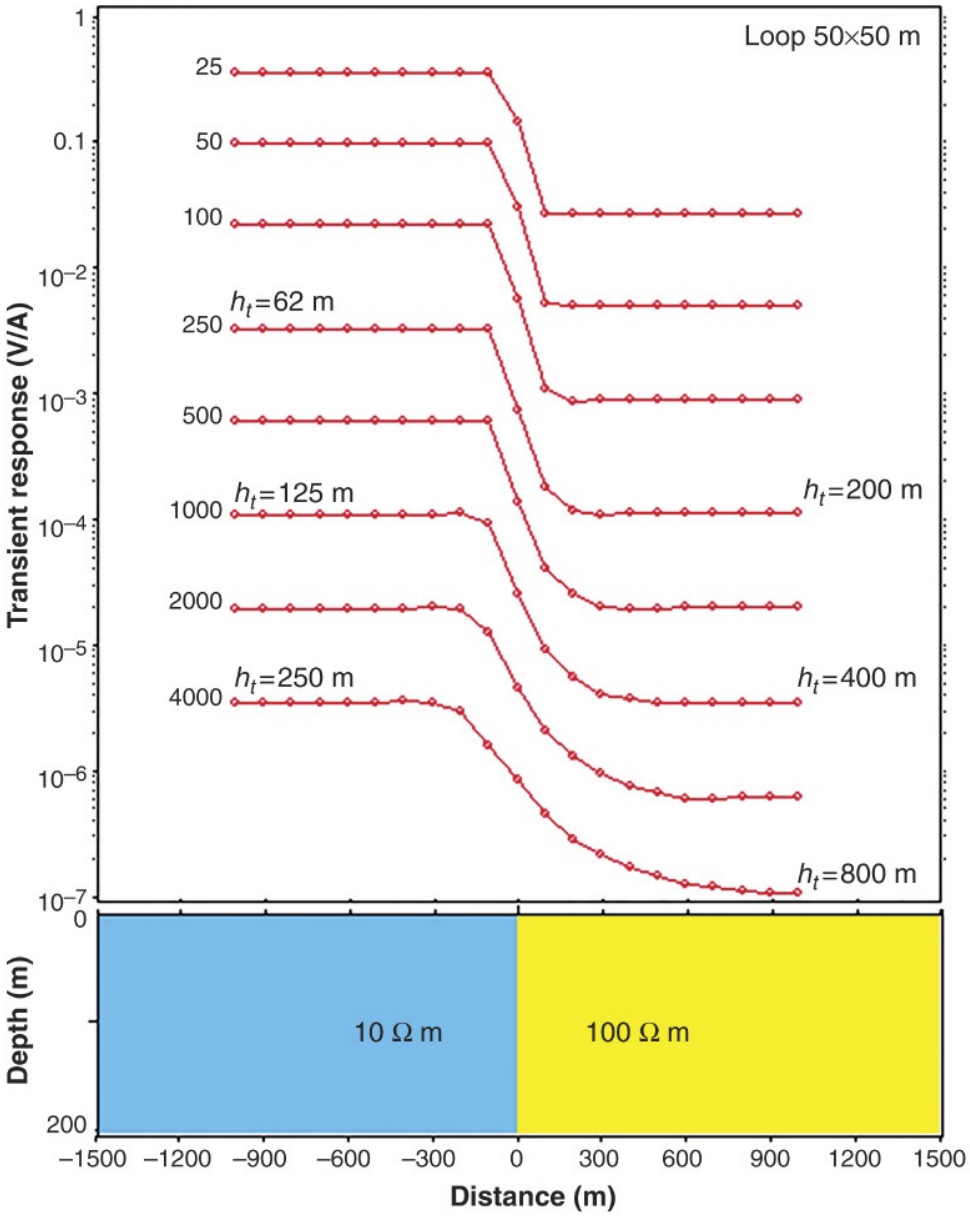

FIGURE 3.12 The transient responses of the vertical contact between two uniform half-spaces: (10 and 100 Ωm) versus distance from border. The labels show the transient time (μs) and diffusion depth h_t in the left and right half-space.

difficulty regardless of the volume and distribution of the initial data. The difficulties arise at the final step of 3-D inversions, when, after construction of the geometrical skeleton of the model, it is required to specify a finite set of resistivities to minimize the misfit between the observed and the model responses. Even assuming that the desired set of resistivities (the parameters of the inversion) comprises hundreds of elements, this does not help. That is why we search for a solution in the class of 2-D or 3-D models composed of the geologically plausible blocks of convenient form and size.[2]

2. Note that the resulting resistivity model is composed of the blocks with the same resistivities as in the prior palette. This limitation of the proposed approach could be overcome in the framework of the 3-D Bayesian statistical inversion (Spichak et al., 1999). (Ed.)

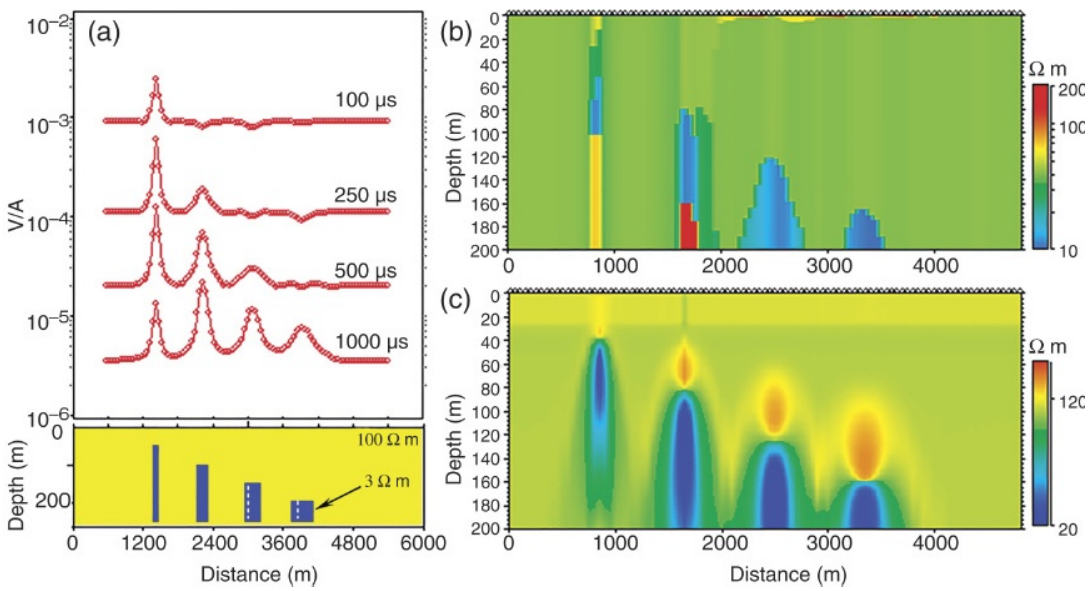

FIGURE 3.13 (a) The transient responses of the vertical pipe models with horizontal section of 100 × 100, 200 × 200, 300 × 300, and 400 × 400 m^2; (b) 1-D inversion; and (c) transformation.

As mentioned earlier, reconstructing the electric structure of the medium from the responses measured on the surface is an ill-posed problem, and its solution requires regularization methods. In the case discussed, the role of regularization is played by the fact that the geometrical skeleton of the model is specified and the set of resistivities of the blocks composing the sought 3-D structure is restricted. Expanding the set of resistivities in order to increase the degree of detail in the sought model makes the solutions unstable and ambiguous. Indeed, the residual probably decreases and becomes uniformly distributed along the profile (or over the surface); however, if not artificially controlled manually, the result of the inversion will depart increasingly farther from the geologically acceptable solution. In practice, acceptable results of the inversion on short profiles or relatively small areas can be achieved in the case if the measured responses are closely electromagnetically coupled with each other. If, however, the profile cuts several geological structures, then, for obtaining a satisfactory result, the 3-D inversion separately for different parts of the profile is carried out with following stitching the model by manual constructing the contact zone of the fragments. Figures 3.14–3.16 illustrate this approach to 3-D inversion of TEM-FAST survey data (Arkhangelsk, Russia). All area under investigation was covered by a regular grid of 100-m antennas (Figure 3.14). The revealed TEM anomalies were detailed along the profile with antenna of 50-m size.

The pointwise 1-D inversion described in Section 3.5 is the first step of 3-D inversion. All results of 1-D inversions were combined to a 3-D model. As example, two resistivity maps and section from this 3-D model are presented in Figures 3.14 and 3.15a.

The maps show that the local anomaly (Figure 3.14a) with a minimum resistivity about 60 Ωm is clearly seen against 250 Ωm host rocks background. However, in a deeper horizon (Figure 3.14b) the anomaly becomes blurred and

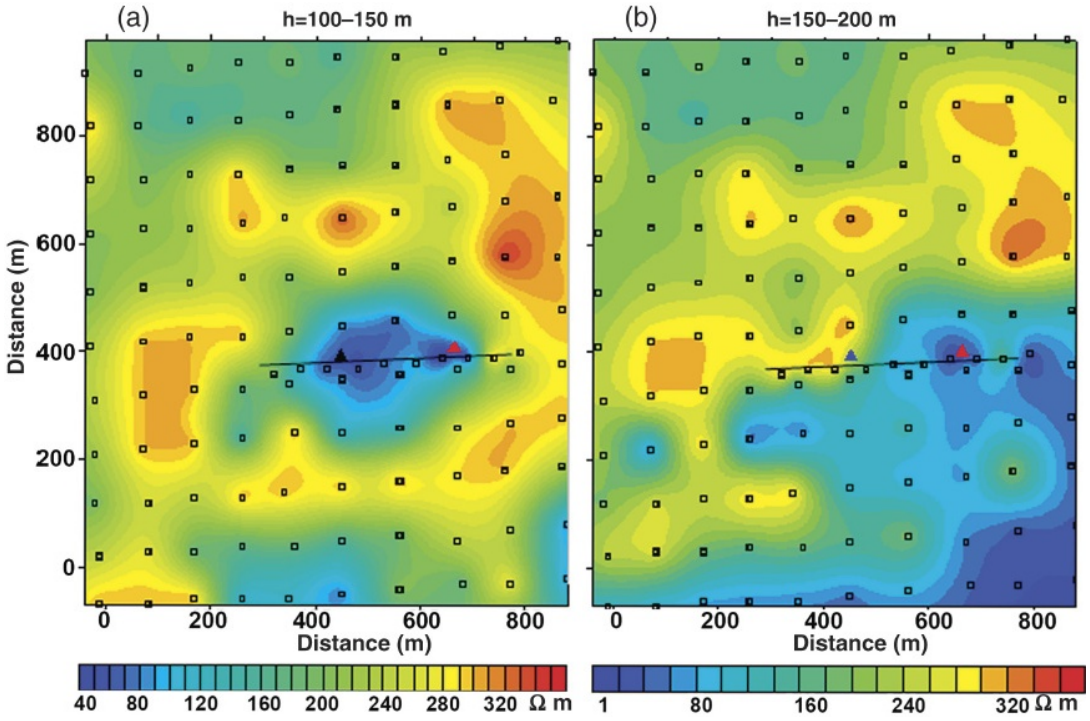

FIGURE 3.14 The maps of resistivity constructed for the rock layers deposited within (a) 100–150 m and (b) 150–200 m depth intervals constructed on the basis of 1-D inversion of array TEM-FAST data. Red and blue triangles and black squares denote wells and centers of antennas of 100×100 m^2 and 50×50 m^2 size, respectively; black line shows profile (W-E direction) through the anomaly.

has resistivity ~100 Ωm against 200 Ωm background. Such structure and magnitude of anomaly does not prove the existence of well conductive target (pipe), it looks rather as local variations of electric properties of the bearing strata. Figure 3.15a shows the section along the profile passing through W1, W2 wells. The conductive block encircled by a thin black line was selected manually as the main target to be detected.

Second step was 1-D pointwise transformation of all data over the survey area, the results of transformations were combined in 3-D model. Figure 3.15b shows the section along W1-W2 profile. As it is seen in Figure 3.15a,b, the minimal resistivity in both wells is 3–10 times less than in 1-D transformation and 1-D inversion cases.

Third step was 3-D inversion. The resistivity of the model was determined in such a way as to fit the calculated responses of the 3-D model to all experimental data over survey area. The same scheme (3.7) was used at this stage. Figure 3.16 illustrates the quality of the inversion: the experimental apparent resistivity curves (triangles) are compared with the model curves calculated for the final 3-D model. The misfit didn't exceed the standard deviation of the experimental data over the whole area. The section of resistivities along the W1–W2 profile is shown in Figure 3.15c. As can be seen, the resistivity values much better agree with the logging data.

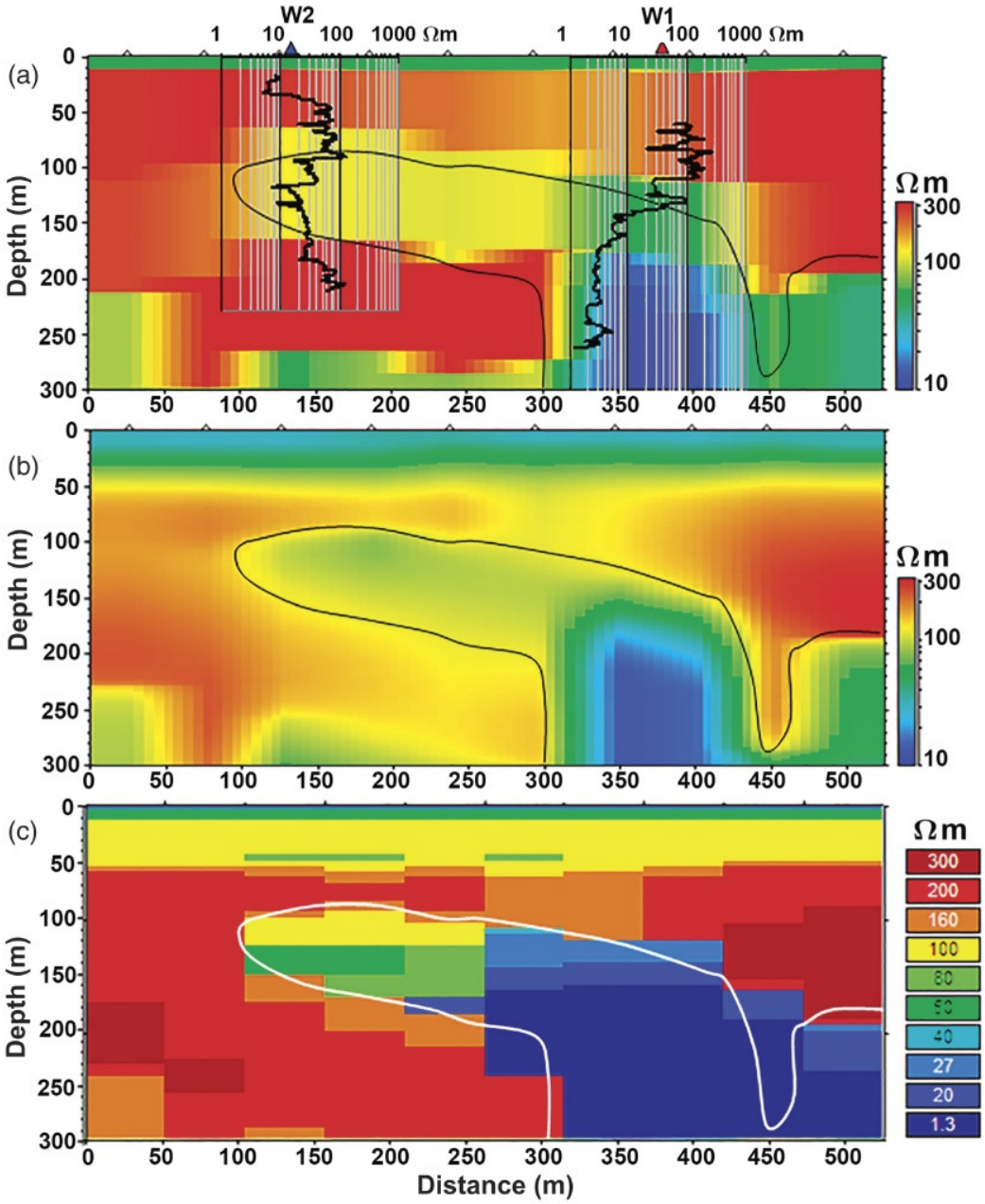

FIGURE 3.15 The resistivity sections along the profile passing through W1 and W2 wells: (a) 1-D inversion, (b) 1-D transformation, (c) 3-D inversion. W1 and W2 show location of the wells; the curves are well logging resistivity versus depth. The contour is the boundary of the resistivity's anomaly determined according to the transformation.

3.6 JOINT INVERSION OF TEM AND DC SOUNDINGS

As it has been already noted, DC soundings are very sensitive to resistive layers and structures imbedded in section, and insensitive to the conductive layers. Quite the contrary, TEM is sensitive to conductive layers and insensitive to the resistive ones. The resolution of both methods can be improved by joint inversion of both DC and TEM data in 1-D class of layered sections providing construction of a single model satisfying all experimental data. Essential property of the way is interactive fitting of parameters of the section.

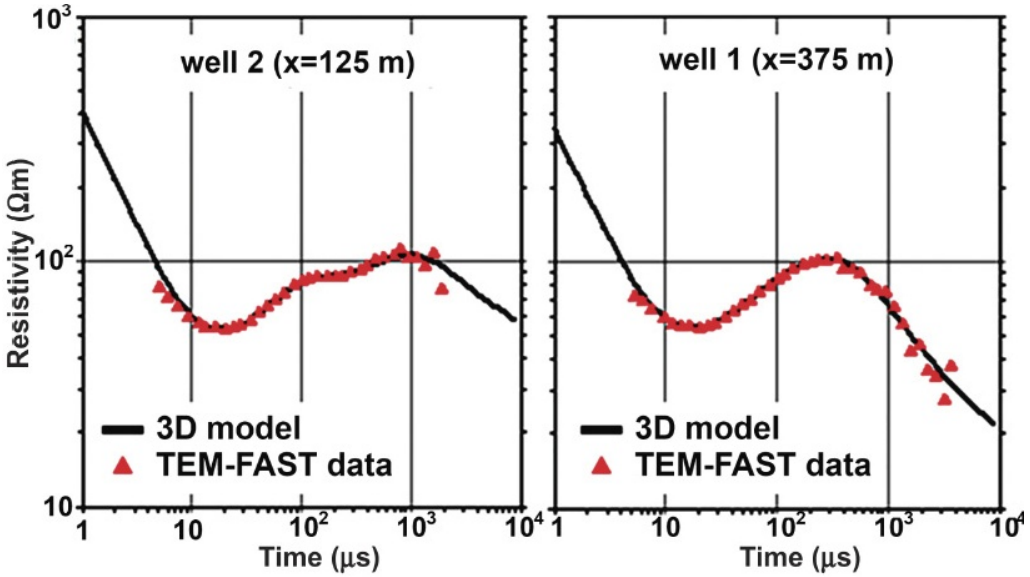

FIGURE 3.16 Comparison of the experimental and calculated apparent resistivity curves in the W2 and W1 well points.

The problems arising at interpretation of TEM sounding data are well known:

- weak sensitivity of the method to the poor conducting layers and rock blocks;
- loss of an information about subsurface layers in the hole zone of early TEM times.

DC soundings meet some problems as well, namely:

- shielding effects present even in thin high-resistance layers limit the depth and resolution of soundings;
- great extent of equivalence of the models obtained at the data inversion;
- ineffective ratio between sounding depth and the size of remote electrode.

However, combined use of both methods is capable to enrich the advantages of each separate method and to decrease essentially their imperfections.

The developed tool for TEM and DC data inversion is based on the analysis and joint inversion of both TEM and DC data in the class of layered sections. Joint inversion implies finding the minimum of misfit functional

$$\Omega = \alpha\|\rho_{DC} - R_{DC}\| + (1-\alpha)\|\rho_{TEM} - R_{TEM}\|, \quad \|\rho - R\| = \sum\left(\frac{\rho - R}{\rho}\right)^2 \exp(-3\Delta/\rho), \quad (3.8)$$

where ρ_{DC} and ρ_{TEM} are experimental values of apparent resistivity for DC and TEM methods, R_{DC} and R_{TEM} are the model values corresponding to 1-D layered model of the section similar for both methods, $\|\cdot\|$ is the norm determined by the experimental data on apparent resistivity and their errors, $0 \le \alpha \le 1$ is the factor defining the contribution of each method in the functional Ω. In case of

TEM, the errors determining the norm $\|\cdot\|$, are calculated directly during field measurements, and for DC – from the results of measurements with fixed center of soundings and various orientation of AMNB line, Δ is a measurement error for time t (TEM); summation is carried out over all t and offsets AB.

The robust technology is applied for suppressing the "heavy tails" of measurements in order to decrease the weight of poor-quality measurements in the functional Ω. In the minimization process the factor α in (3.8) changes smoothly from 1 to 1/2 (or from 0 to 1/2), which allows avoiding local minima of the functional. In the beginning, a model adequate to the data provided by either a single TEM or a single DC method is used as the initial model; then the model parameters gradually and interactively change the data on the basis of both methods. This strategy is an essential element of the process of the problem solution. 2-D and 3-D geological structures are thus represented as the geoelectric images constructed like tomograms on the base of local 1-D TEM and DC inversion adjusting the data of profile or array measurements. Examples of such an analysis and inversion are shown in Figures 3.17 and 3.18.

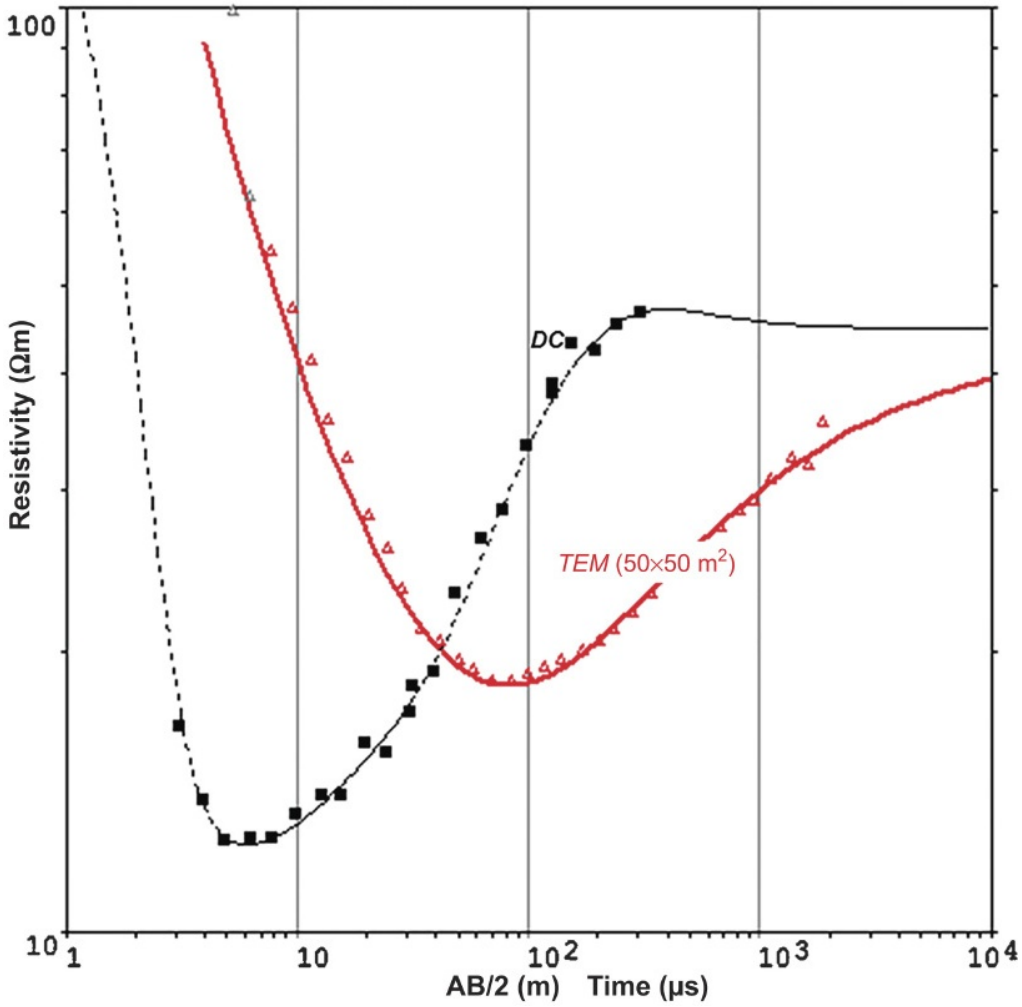

FIGURE 3.17 Joint inversion of TEM and DC data with the modeling curves of apparent resistivity.

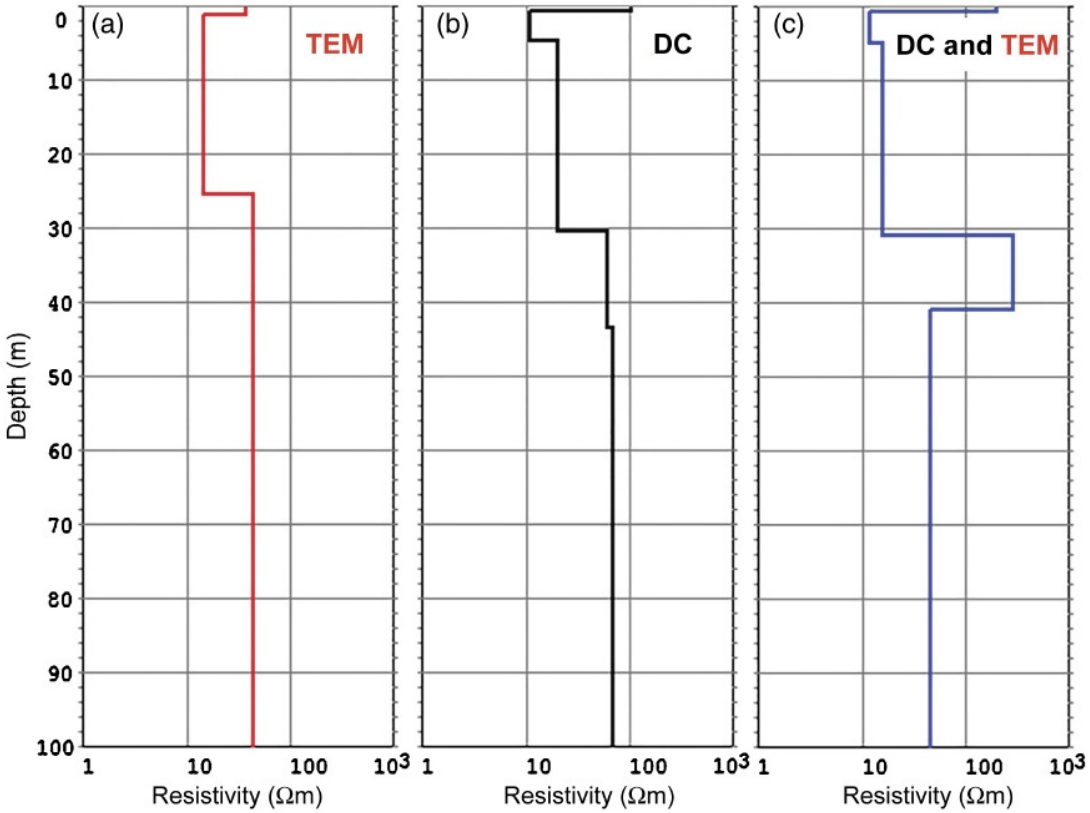

FIGURE 3.18 The results of DC and TEM-FAST inversion (Crete, Greece): (a) only TEM, (b) only DC, (c) DC and TEM jointly. DC and TEM responses are shown in Figure 3.17.

Figure 3.17 shows the measured data and the results of an individual and joint inversion, and Figure 3.18 presents the corresponding sections for:

1. separate TEM ($\alpha = 0$), (one-loop 50×50 m^2 configuration);
2. separate DC ($\alpha = 1$), (Schlumberger configuration MN = 2 m);
3. TEM and DC data together, ($\alpha = 1/2$).

In separate inversions the misfit (mean square deviation) between the model and experimental data is minimal and falls within the confidence limits of the error. In the case of joint inversion, this misfit is certainly higher, however it is still within the confidence interval. As one can see, in spite of the model and experimental curves of apparent resistivity being quite close in case of separate inversions, the obtained sections are rather far from the real geological data. In joint inversion, the result is quite adequate to the real geological section.

Example of practical applications of the earlier-described technology of joint inversion in hydrogeological prospecting is presented by Figure 3.19. A 5-km long profile goes along the Nile (Egypt); the purpose of this survey was water springs prospecting. The geological structure is characterized by inter-bedding of limestone (head water horizon) and clay (confining layer). A good agreement of sounding and well data is seen in Figure 3.19.

Several other examples illustrating an application of TEM-FAST technology for hydrogeological research are shown subsequently. Figure 3.20 illustrates

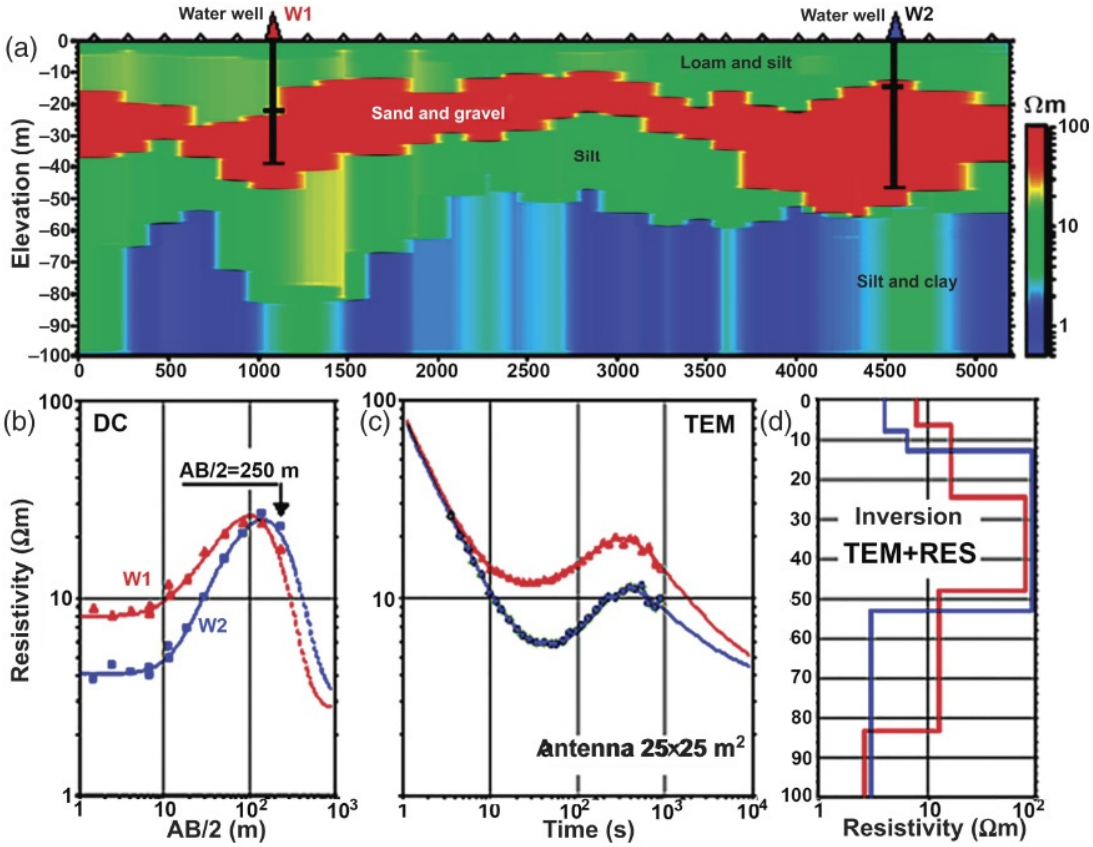

FIGURE 3.19 Joint TEM and DC inversion (Nile, Egypt). (a) the resistivity section along the Nile; W1 and W2 – are the water wells; (b) and (c) comparison of the measured DC (b) and TEM (c) data (dots) with the inverted model data (curves) in the wells' points. (d) The layered section in W1 and W2 pints according to joint TEM-DC inversion.

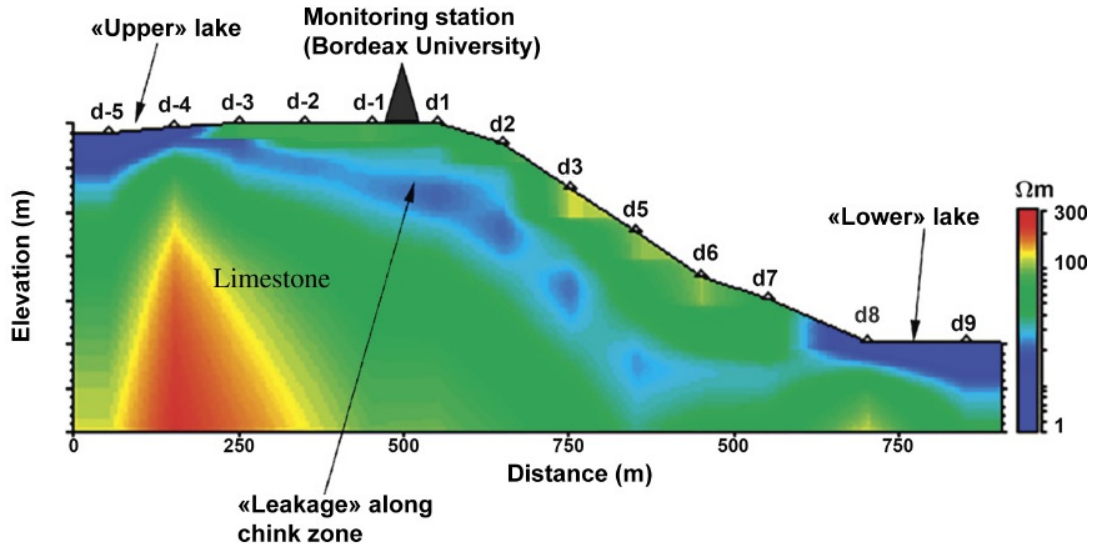

FIGURE 3.20 Study of the fracture zone (French Alps). The low resistivity area (blue color, ~10 Ωm) indicates the area of water leakage from upper lake to low one.

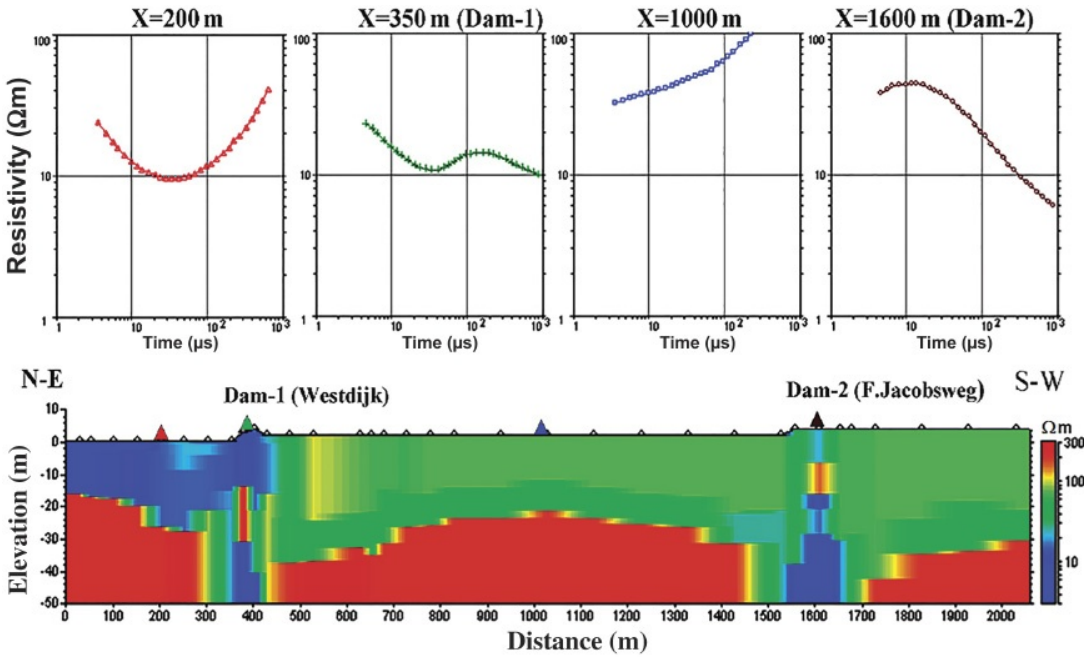

FIGURE 3.21 Geoelectric section across a protecting dam (the Netherlands). Upper panel shows the apparent resistivity curves in points X = 200, 350, 1000, 1600 m along the profile. Conductive (blue color) areas indicate the water leakage path.

high resolution of TEM sounding in solving the problems of ground water leaking in Grenoble (French Alps). Such problems arise in regions of water storage reservoirs used for city water supply or energy production. At data analysis and interpretation the above-described technology of data transformation was applied. In spite the dam, the water leaks from upper reservoir to the lower one.

Considerable part of the Netherlands is separated from the North Sea by dikes. From time to time, the dykes are destroyed by pouring rains and sea pressure, therefore the monitoring of dams' state is of great importance. As seen from Figure 3.21, TEM-FAST provides a good opportunity to monitor the dikes condition.

The apparent resistivity curves are shown in the upper part of Figure 3.21. They give an impression on quality of the measured data in some points and cross-section in these points. There are two dams located at the distance of 1200 m. The main part of the water is blocked by first dam, some part of the water achieves second dam and is accumulated under it.

3.7 SIDE EFFECTS IN TEM SOUNDING

In practical, TEM-FAST applications, as well as other TEM methods though, three physical phenomena take place that complicate the process of field diffusion and may affect considerably the effectiveness of geological interpretation of the measured results:

- superparamagnetic effect (SPM effect),
- effect of induced polarization (IP effect),
- antenna polarization effect (AP effect).

Depending of the problem at hand, these effects can be treated as "harmful" or "useful" carrying an additional information about the medium under study.

3.7.1 Superparamagnetic Effect in TEM

SPM or effect of magnetic viscosity, has been studied by many researchers (Neel, 1950; Nagata, 1961; Averianov, 1965; Buselli, 1982; Barsukov and Fainberg 2001, etc.). SPM effect in rocks is related with processes of orientation/disorientation of magnetic moments of very fine (of the order of an Angstrom) grains of magnetic minerals at initial moments of off/on switching of the exciting magnetic field. TEM-FAST studies of the SPM effect in different regions of the world show that the most intensive SPM effects are observed in regions of effusive and volcanogenic-sedimentary rocks development, the most SP formations being the subsurface clays covering the parent rock masses. SPM effects are encountered in permafrost conditions and are usually localized at the boundaries of the frozen rock thaw. Considerable SPM effects are observed in glaciers. SPM is generated, as a rule, by magnetite and maggemite particles of $\sim 10^{-9}$–10^{-7} m size. SPM effects are usually understood as a frequency dispersion of magnetic susceptibility of rocks (on the analogy with frequency dispersion of conductivity or IP phenomena).

To identify SPM in the measured data, a function $t \cdot E(t)$ is provided in the TEM-FAST system interface. Later stages of the transient process containing SPM component, when multiplied by t, give a function almost constant in time. In practice, due to various reasons, against the Neel (1950) theory, the observed SPM processes decrease as $E \sim 1/t^{1+\delta}$, where $-0.2 < \delta < 0.2$. For coaxial circular antenna, located above a SP half-space at height h, SPM transient processes are described by formula (Averianov, 1965):

$$\frac{E(t)}{I} = \mu_0 \cdot \chi_{\mathrm{SPM}}(t) \cdot F(R,r,h)$$

Geometric function, F is equal to $(R,r,h) = 1/2 \cdot (R \cdot r)^{1/2}\, Q_{1/2}(x)$ where $Q_{1/2}(x)$ is the Legendre function of the order of ½ with argument $x = (4h^2 + r^2 + R^2)/2rR$. Here R and r are size of the transmitting and receiving antennas. In case of coincident antenna configuration at $R = r$ and small $h/R << 1$, geometric function is proportional to the antenna perimeter $F(R,R,h) = 1/2 \cdot R \cdot ln(R/h)$, and at $R = r$ and $h = 0$ F is equal to the antenna inductivity L. At $r < R$ and $h = 0$ function F is equal to mutual inductivity of antenna M. With a decrease of the receiving antenna size, function F drops abruptly within an interval $1 > r/R > 0.9$, and further on approaches its asymptote proportional to the area of the receiving antenna $F(R,r,h) \sim r^2$.

Precise calculations of transients for horizontally layered conductive and SP medium show that the interaction between induction currents in the medium and SPM effects is negligible, that is, these effects can be assumed additive. In order to reduce the SPM effects influence on the sounding results, three approaches

are possible: to lower mutual inductance of antennae M, to increase the size of coincident antenna facility, and to raise the coincident antenna above the medium. Three characteristic features of SPM distortions are as follows:

1. late stages of the process are proportional to $E(t) \sim 1/t$;
2. resistivity $\rho(t)$ drops rapidly down to very low values;
3. curves $\rho(t)$ at later times for different in size antenna show steeply falling parallel branches.

To avoid problems associated with SPM effect, one has to check the measured data for a distortion and to change the antenna configuration if necessary. At the same time, SPM can be used also in analyzing the magnetic properties of rocks and in prospecting of ore deposits accompanied by SPM anomalies in their overlaying soils. This possibility arises from the SPM effect properties.

Chunhan et al. (1997) have experimentally studied the gas bubbles with the nitrogen, oxygen, argon, and methane being the major components within them. These volatiles are generated mainly by the gas breath of the mantle. The gaseous agents are continually moving from the depth to the surface, influenced by many factors, mainly the pressure. Studies of the gas aureole showed that the gas flows can transport the metallic particles in vertical direction both at high and at atmospheric temperatures. Analytical technique of electron microscopy made it possible to find that the gas emanating from the earth contains Si, Al, K, Na, S, and also several content of Fe, Mg, Ti, V, Zn, Au, As, Ba, Ca, etc. Just these elements are responsible of the SPM effect. Some examples of successful analysis of emanating gas fluxes as applied to ore prospecting in fault zones were described in (Kristiansson et al., 1990).

The results of measurements of SPM-effects on a structure through rich stream-gold are presented in Figure 3.22 (soil samples are taken from South Ural). The deposit is located at a depth of about 40 m and covered by a layer of terrigenous sedimentary rocks. For the analysis, samples of superficial clay (volume of 1.5 L) were extracted from a depth of 20 cm and after drying positioned in the cavity of a special high-sensitivity SPM-sensor manufactured as a hollow toroid.

After measurements of SPM-susceptibility χ_{SPM}, an additional parameter δ which is the small increment in the power law index of the measurements $E(t) \sim l/t^{1+\delta}$ was determined (Barsukov and Fainberg, 2001). As one can see from the Figure 3.22, both conventional parameters of magnetic susceptibility χ_{magn} (Figure 3.22a) and χ_{SPM} (Figure 3.22b) don't indicate existence of any anomaly, at the same time parameter δ shows clearly local anomaly. It should be mentioned that SPM effect does not allow determination of the occurrence depth of the object in such a way as it is done in induction prospecting, but it exceeds the latter in horizontal resolution.

Other example of TEM-FAST research with SPM application is shown in Figure 3.23 that displays the results of questing a large bombe, mine, and shell arsenal left in adits of Sevastopol since the Second World War. The adits lie

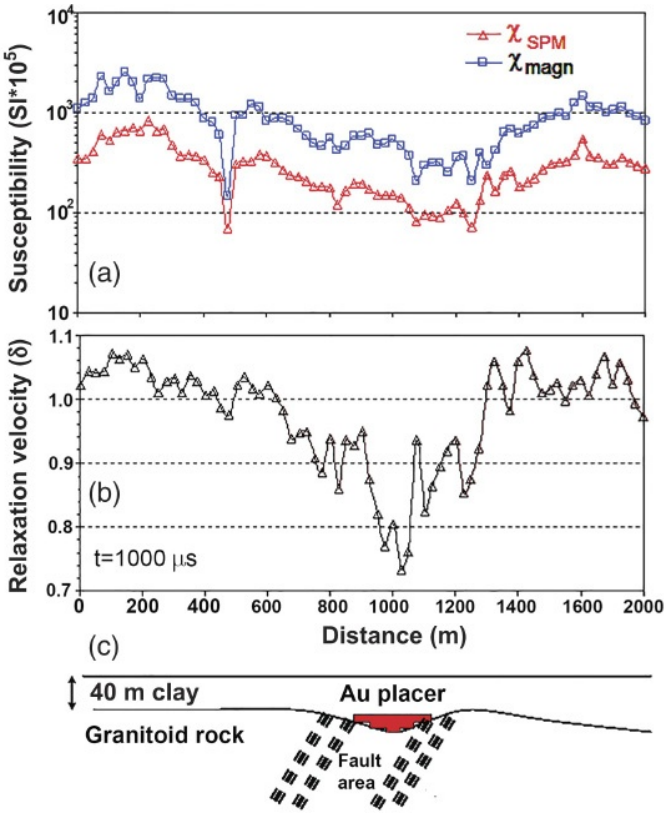

FIGURE 3.22 SPM effect over the gold placer. (a) magnetic susceptibility χ_{mag} measured with a viscometer, and SPM susceptibility χ_{SPM} measured with a solenoid, (b) relaxation velocity parameter δ.

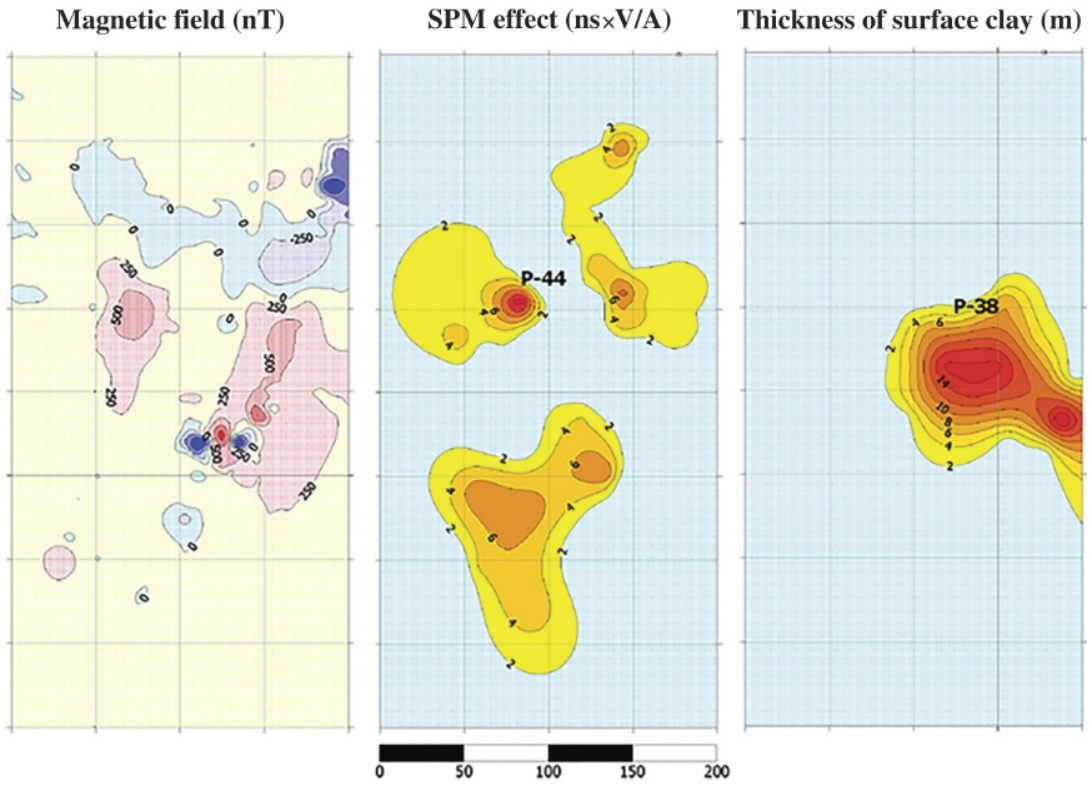

FIGURE 3.23 Comparison of traditional and alternative (SPM) research of underground adits.

at a depth more than 25 m and are overlain by a thick layer of highly conductive clay.

As seen from the left panel of Figure 3.23, the magnetic survey revealed chaotic distribution of magnetic anomalies. Usual induction sounding does not feel metal objects due to the shielding effect of the clay. At the same time, SPM effect rather well outlines the scheme of ammunition disposition that agrees with the results of speleological studies of the adit passages.

3.7.2 Effect of Induced Polarization

The importance of studying the induced polarization effect results from a wide prevalence of this effect in various geological media and its essential influence on the results of practically all EM studies. Often it is very hard to diagnose the IP effects from TEM field data. The exceptions are cases of very intense manifestations of the polarization at low levels in induction processes when the observed signals more than once invert their sign. Cases occur when the entire observed signal from 4 μs to 4–10 ms has a negative sign. Much more often the polarization process distorts the observed signal but without changing the sign. In the interpretation of these cases, sometimes artifacts of low conductance layers are revealed. Often IP-effect is adequately described by well known Cole and Cole (1941) formula, but in a series of cases this formula is insufficient and it is necessary to involve other considerations, e.g., those by Debye, Davidson, and others (Pelton et al., 1983). As the analysis with TEM-FAST showed, the most unfavorable for interpretation situations where IP effects are manifested as follows:

- thin conductive horizon of subsurface clay deposits with $\rho < 20$–40 Ωm laying at rather high-resistive rock masses with $\rho > 300$–500 Ωm. At a noticeable polarization of this layer, the later stages of transient process are distorted by IP effects;
- glaciers and frozen rocks;
- subsurface deposits highly polluted by industrial waste products (including pollution by oil);
- weathering cores in crystal rocks and fault zones.

As an example of IP effect, we present the results of the research performed by TEM and DC method carried out on the Sphinx-pyramid Chephren area. The purpose of the research was to evaluate the configuration of aquifers and groundwater reservoirs. The studies started initially as purely geological, however, led to unexpected result: between the famous objects the Sphinx, Cheops, and Chephren pyramids, a region with abnormally high electrical conductivity have been found. Conventionally, this region was believed associated with cavities in limestone formations of the Giza plateau that contain mineralized water and have rather low resistivity. In the year 2000, deep underground galleries were discovered at this site. Intensive IP effect was revealed near the Chephren

pyramid where according the TEM-FAST measurements the local fault does exist. The area under investigation is shown in Figure 3.24 and details of IP effect are shown in Figure 3.25.

After detection of IP effect no further studies in this regard have been conducted, so the nature of the local zone of intense polarization effect at the foot of the Chephren pyramid remains still a mystery.

Analysis of experimental data and numerical modeling of TEM soundings distorted by polarization effect showed that in most cases the source of distortions is shallow rocks. The resistivity of these rocks is less than 20–40 Ωm, the depth does not exceed 1–2 m, and their "background" polarizability η is less

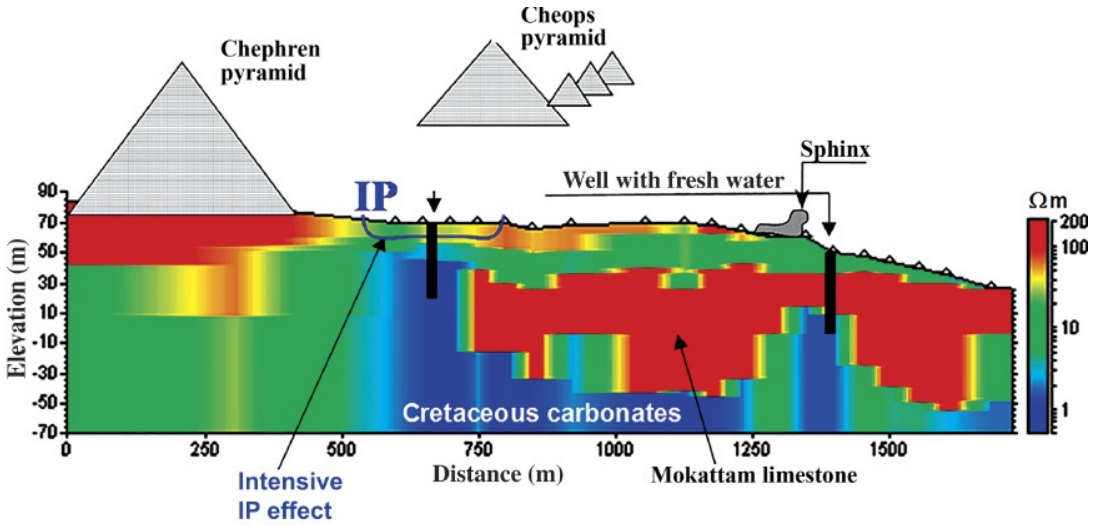

FIGURE 3.24 The electric cross-section under the Great Egyptian Pyramids plateau (Giza, Egypt) and location of IP effect.

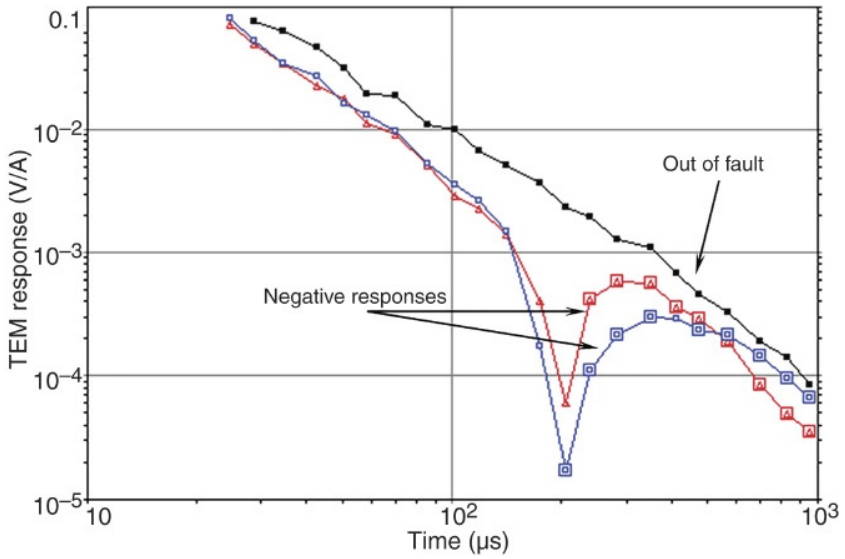

FIGURE 3.25 IP effect in the fault zone in the area of the Cheops and Chephren Pyramids. The blue and red curves are measured on both sides of the fault and the black curve away of the fault.

than 1–3%. The polarization effects of rocks with $\rho > 100$ Ωm appear only at considerably high polarizability $\eta > 10\%$; time constants τ_{ip} lie within a very wide range of 1–1000 μs. For surface IP effect, usually c is about 1 and distortions are observed within a narrow time interval. Deep IP-effect is characterized by c of about 1/3–1/2 and distorts all the later stages of the signal. If the sources of IP-effect are both in subsurface and deep horizons of a rock mass, two negative minima are observed at earlier and later times.

It should be noted that since the IP effect speaks for the presence of polarizable bodies or fluids, it can be used in the prospecting, tracing, and monitoring these objects.

3.7.3 Antenna Polarization Effect

Antenna polarization effect has been detected in the TEM data by many researchers (see for instance, Bishop and Reid, 2003) but only recently an explanation to this effect was found. In practice, transient responses (or their time derivatives) often change the polarity, which is due to the frequency dependence of electrical conductivity of rocks. In induction electric prospecting, these effects are called "negative anomalies." Figure 3.26 demonstrates an example of such "anomalies."

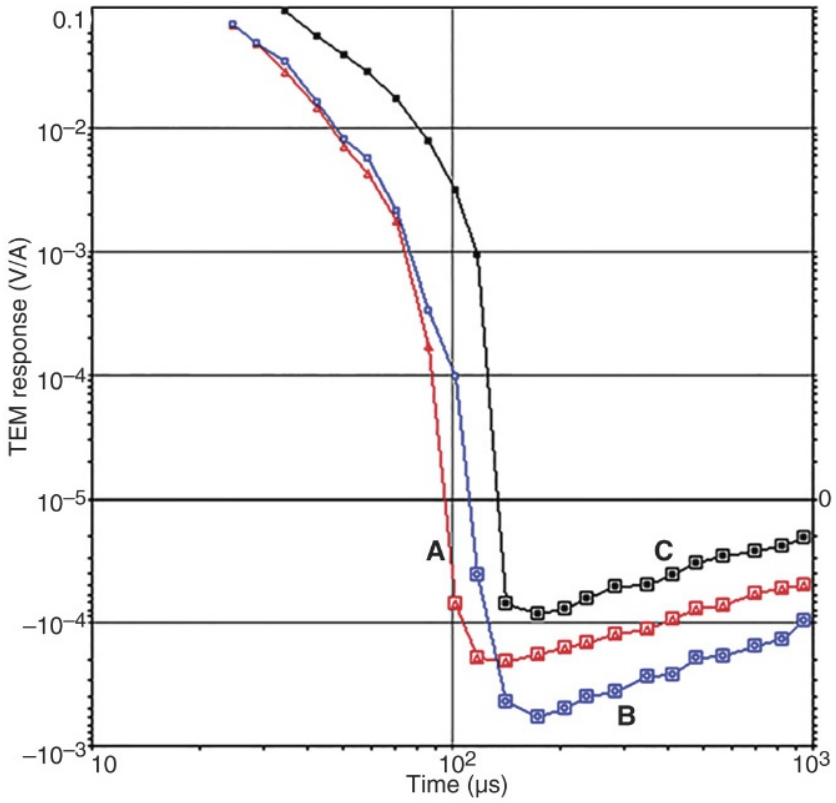

FIGURE 3.26 Negative in-loop TEM decays from A to C point. The point A is located on outcropping granite, the overburden thickens progressively with distance from A toward B and C points.

Theoretically, it is not difficult to calculate transient characteristics of horizontally layered media with conductivities described by complex frequency-dependent function (e.g., Cole–Cole formula).

Comparison of experimental data with the calculated in such a way transient characteristics shows that discrepancies are often observed that do not fit theoretical models of polarizable media, for example, the value of negative anomalies depends on the resistivity of the antenna wire. These discrepancies between the experiment and theory cannot be explained by horizontal inhomogeneity of the medium or imperfection of the modeling technique. It is obvious that the interpretation algorithms in such cases face insuperable difficulties. Numerous field experiments and theoretical analysis of this effect based on the antenna system consideration as a line with distributed parameters allowed the conclusions to be made as follows.

Distributed antenna capacity and resistance ever persisting in real devices employed in the study of geological media with frequency dependent dielectric permeability produces the antenna polarization effect. This effect shows at later stages of transient process and is detected as a slow decaying with time process $\sim 1/t^{(0.3–0.7)}$ with its phase opposite to the phase of induction transient characteristics. Antenna polarization effect depends on the dispersion parameters of the medium and, with a fixed current, is proportional to the squared resistivity of the antenna wires. Distributed resistivity of antenna circuits where the currents run even in case of symmetric rotation of the antenna-medium system produces asymmetric electric fields with radial and vertical components. Antenna polarization effect is detected in both the coincident receiving–transmitting and the spaced antenna and should be taken into account in the field data interpretation. The results of field experiments that prove the dependence of antenna polarization effect on the resistivity and capacity of antenna's wires are shown in Figures. 3.27 and 3.28.

These experiments also showed that the simplest and the best way against the antenna polarization effect is surveying using the antenna cable with good insulation.

3.8 CONCLUSIONS

The technology of pulsed electromagnetic soundings allowing exploring the geological media in the depth range from a few meters up to 300–500 m with the maximum possible vertical and lateral resolution is considered. It is shown that using a coincident transmitting-receiving antenna of 10–500 m size for measureme nt of transient responses provides high performance and cost efficiency studies. Preprocessing of the field data are carried out synchronously with the measurement process under the strict control.

Preliminary interpretation of the measured responses is produced in the form of resistivity versus depth dependency directly in the field, which allows adjusting the strategy of surveying to get highest possible information on the medium under prospecting.

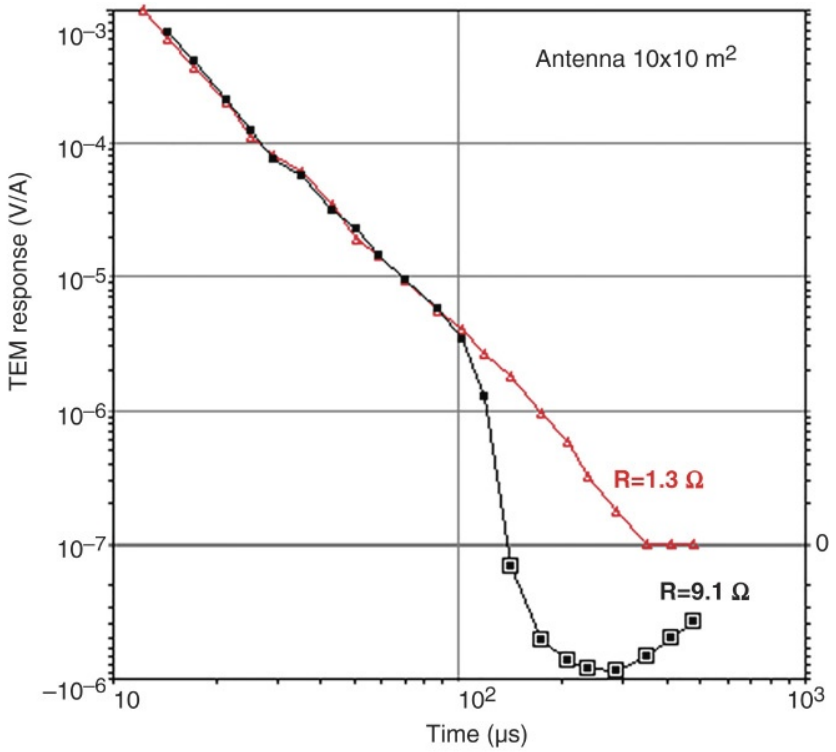

FIGURE 3.27 Dependency of the signal in a coincided antenna on the "ground-wire" resistance. Labels on the curves show the resistance of the loops.

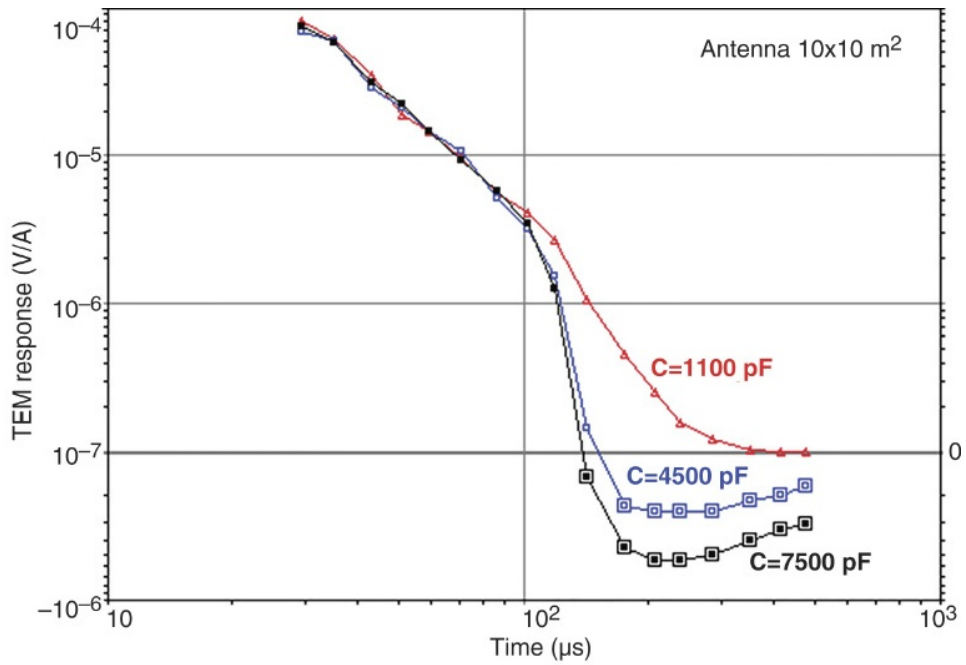

FIGURE 3.28 Dependency of the signal in a coincided antenna on the "ground-wire" capacitance. Labels on the curves show the capacitance of the loops.

The measured TEM responses are transformed into 1-D resistivity models by local transformations and 1-D inversions, and then are "stitched" into 2-D or 3-D pseudo-sections. As a rule, these pseudo-models adequately represent the main features of the investigated medium.

At the final stage, 10–15 large blocks in the pseudo-models are allocated, they used as the starting blocks for 3-D inversion. The resistivity of these blocks is determined by minimizing the residual between the observed and model responses. At the final stage of the inversion, the program complex, based on effective finite-difference code for 3-D direct problem solution and interactive interface allowing to adjust the graphically selected blocks of rocks, and to compare online the observed and calculated transient responses, is used.

The possibility of joint inversion and interpretation of TEM and DC soundings allowing distinguishing the local high resistive targets that do not reveal in the transient responses, as well as the local conductive targets that do not reveal in the DC methods was demonstrated.

Some side effects arising at TEM-FAST investigations are discussed. It is shown that in some cases the TEM-FAST technology can effectively explore the geological media consisting of rocks having frequency dispersion of conductivity and magnetic susceptibility. Several examples of SP effects used for such studies are demonstrated.

REFERENCES

Averianov, V.S., 1965. Role of magnetic crystallographic anisotropy in the process of viscous magnetization of ferrites. Izv. Phys. Earth 7, 82–89.

Barsukov, P., Fainberg, E., 2001. Superparamagnetic effect over gold and nickel deposits. Eur. J. Environ. Eng. Geophys. 6, 61–72.

Berdichevsky, M.N., Dmitriev, V.I., 1992. Magnetotelluric sounding of horizontally-uniform media (in Russian). Moscow, "NEDRA", p. 250.

Bishop, J., Reid, J., 2003. Some Positive Thoughts About Negative TEM Responses. ASEG 16th Geophysical Conference and Exhibition, Adelaide.

Buselli, G., 1982. The effect of near-surface superparamagnetic material on electromagnetic measurements. Geophysics 47 (9), 1315–1324.

Chunhan, T., Juchu, L., Liangquan, G., 1997. Nano-scale particles of ascending gas flows in the crust and geogas prospecting. Engineering and environmental geophysics for the 21st century. Proceedings of the International Symposium, Chengdu, China, Sichuan Publishing house of Science and Technology, pp. 337–342.

Cole, K.S., Cole, R.H., 1941. Dispersion and absorption in dielectrics. I. Alternating current field. J. Chem. Phys. 9, 341–351.

Commer, M., Hordt, A., Helwig, S., Scholl, C., 2003. Three-dimensional inversion of time-domain EM data with highly constrained model complexities. 20 Kollokuium elektromagnetische tiefenforschung, Konigstein, pp. 114–123.

Druskin, V., Knizhnerman, L., 1988. A spectral semi-discrete method for the numerical solution of 3-D non-stationary electric prospecting problem. Phys. Solid Earth 24, 641–648.

Gubatenko, V.P., Tikshaev, V.V., 1979. On changes in the sign of electromotive force of induction in the transient electromagnetic field method (in Russian). Izv. Phys. Earth 3, 95–99.

Kamenetsky, F.M., Stettler, E.H., Trigubovich, G.M., 2010. Transient Geo-electromagnetics. GEOS, Munich, p. 304.

Kristiansson, K., Malmquist, L., Persson, W., 1990. Geogas prospecting: a new tool in the search for concealed mineralization. Endeavour New Series 14 (1), 407–416.

Lee, T.J., 1981. Transient EM response of a polarizable ground. Geophysics 46 (7), 1037–1041.

Nagata, T., 1961. Rock Magnetism. Plenum Press, New York, p. 350.

Neel, L., 1950. Theorie du trainage magnetique des substances massives dans le domaine le Rayleigh. J. Phys. Radium 2, 49.

Obukhov, G.G., 1968. About some properties of the nonstationary electro-magnetic fields in the earth and their applications in electrical prospecting. Izv. Phys. Earth 9, 62–71.

Pelton, W., Sill, W., Smith, B., 1983. Interpretation of complex resistivity and dielectric data. Geophys. Trans. 29 (4), 297–330.

Schlumberger, C., 1920. Etude sue la prospection electrique du sours-sol. Gautier-Villars Cie, Paris.

Sidorov, V.A., Tikshaev, V.V., 1969. Electrical Prospecting with Transient Field in Near Zone. Saratov University Press, Saratov.

Spichak, V.V., Menvielle, M., Roussignol, M., 1999. Three-dimensional inversion of EM data using Bayesian statistics. In: Spies, B., Oristaglio, M. (Eds.), 3D Electromagnetics. SEG Publ., GD7, Tulsa, USA, pp. 406–417.

Svetov, B.S., Barsukov, P.O., 1984. Transformation of quasi-stationary geoelectric transient processes into equivalent wave processes (in Russian). Izv. Phys. Earth 8, 29–37.

Weidelt, P., 1982. Response characteristic of coincident loop transient electromagnetic system. Geophysics 47 (9), 1325–1330.